The Astrophysical Journal, 911:3 (21pp), 2021 April 10 https://doi.org/10.3847/1538-4357/abe620

Downstream Depolarization in the Sausage Relic: A 1–4 GHz Very Large Array Study

G. Di Gennaro[1,2], R. J. van Weeren[1,2], L. Rudnick[3], M. Hoeft[4], M. Brüggen[5], Dongsu Ryu[6], H. J. A. Röttgering[1], W. Forman[2], A. Stroe[2,8], T. W. Shimwell[1,7], R. P. Kraft[2], C. Jones[2], and D. N. Hoang[5]
[1] Leiden Observatory, Leiden University, PO Box 9513, 2300 RA Leiden, The Netherlands; digennaro@strw.leidenuniv.nl
[2] Center for Astrophysics |Harvard & Smithsonian, 60 Garden Street, Cambridge, MA 02138, USA
[3] Minnesota Institute for Astrophysics, University of Minnesota, 116 Church Street SE, Minneapolis, MN 55455, USA
[4] Thüringer Landessternwarte, Sternwarte 5, D-07778 Tautenburg, Germany
[5] Hamburger Sternwarte, Universität Hamburg, Gojenbergsweg 112, D-21029 Hamburg, Germany
[6] Department of Physics, School of Natural Sciences UNIST, Ulsan 44919, Republic of Korea
[7] ASTRON, The Netherlands Institute for Radio Astronomy, Postbus 2, 7990 AA, Dwingeloo, The Netherlands
Received 2020 June 17; revised 2020 December 7; accepted 2021 February 11; published 2021 April 8

Abstract

Radio relics are elongated sources related to shocks driven by galaxy cluster merger events. Although these objects are highly polarized at GHz frequencies ($\gtrsim$20%), high-resolution studies of their polarization properties are still lacking. We present the first high-resolution and high-sensitivity polarimetry study of the merging galaxy cluster CIZA J2242.8+5301 in the 1–4 GHz frequency band. We use the *QU*-fitting approach to model the Stokes *I*, *Q*, and *U* emission, obtaining best-fit intrinsic polarization fraction (p_0), intrinsic polarization angle (χ_0), rotation measure (RM), and wavelength-dependent depolarization ($\sigma_{\rm RM}$) maps of the cluster. Our analysis focuses on the northern relic (RN). For the first time in a radio relic, we observe a decreasing polarization fraction in the downstream region. Our findings are possibly explained by geometrical projections and/or by decreasing of the magnetic field anisotropy toward the cluster center. From the amount of depolarization of the only detected background radio galaxy, we estimate a turbulent magnetic field strength of $B_{\rm turb} \sim 5.6\ \mu$G in the relic. Finally, we observe RM fluctuations of about 30 rad m^{-2} around the median value of 140.8 rad m^{-2} at the relic position.

Unified Astronomy Thesaurus concepts: Galaxy clusters (584); Galactic and extragalactic astronomy (563); Polarimetry (1278); Intracluster medium (858); Shocks (2086); Plasma astrophysics (1261)

1. Introduction

Radio relics are synchrotron sources generally located in the outskirts of merging galaxy clusters. They are elongated, often arc-shaped, and not associated with any optical counterparts. It is now accepted that these sources trace particles (re)accelerated owing to the propagation of shock waves generated by a cluster −cluster merger event (see Brunetti & Jones 2014; van Weeren et al. 2019, for a theoretical and observational review). Being synchrotron sources, radio relics are also tracers of the magnetic field in cluster outskirts. Numerical simulations (e.g., Dolag et al. 1999; Brüggen et al. 2005; Vazza et al. 2018), as well as observations (e.g., Govoni & Feretti 2004; Bonafede et al. 2010a), show that the magnetic field intensity declines with radius (and hence with particle density) in clusters, with central values of a few μG (Bonafede et al. 2010a). On the other hand, it is expected that, during a cluster merger, the unordered magnetic fields in the intracluster medium (ICM) are compressed, amplified, and aligned with the propagating shock plane, generating strongly linearly polarized emission ($\gtrsim$20%; see Enßlin et al. 1998). The exact mechanism leading to magnetic field amplification at shocks is not completely understood (see Donnert et al. 2018, for a recent review). For the typical low Mach numbers of cluster merger shocks ($\mathcal{M} = 1 - 3$), the amplification factor appears to be too small to explain the magnetic field strength measured in relics simply via shock compression, as it is for supernova remnants (Iapichino & Brüggen 2012; Donnert et al. 2017). Recently, new high-resolution (i.e., 32 kpc) numerical simulations by Wittor et al. (2019) show that the polarized emission from relics should strongly depend on the properties of the upstream magnetic field, with laminar gas flow generating parallel alignment of the electric vectors. Determining the polarization properties of radio relics thus plays a crucial role in the understanding of these sources, as well as the properties of the ICM.

While studies of magnetic fields of radio galaxies, in the field and in galaxy clusters, have been performed (e.g., Bicknell et al. 1990; Govoni et al. 2006; Bonafede et al. 2010b; Frick et al. 2011; Farnsworth et al. 2011; O'Sullivan et al. 2012, 2018; Orrù et al. 2015), very little information is known on the magnetic field structure in radio relics, with few observational studies performed so far (Bonafede et al. 2010a; van Weeren et al. 2010, 2012; Bonafede et al. 2013; Ozawa et al. 2015; Pearce et al. 2017; Stuardi et al. 2019). In this paper, we present a detailed polarization analysis, performed with the Jansky Very Large Array (VLA), of the well-studied merging galaxy cluster CIZA J2242.8+5301 (hereafter CIZAJ2242) at $z = 0.192$ (Kocevski et al. 2007).

The cluster is the result of the collision of two equal-mass subclusters (Dawson et al. 2015; Jee et al. 2015), with a small inclination of the merger axis to the plane of the sky (i.e., $|i| \lesssim 10°$; van Weeren et al. 2011). The cluster hosts two main radio relics, in the north and in the south, several tailed radio galaxies, and several patches of diffuse emission (see Di Gennaro et al. 2018). High-frequency studies, up to 30 GHz, showed a possible steepening in the integrated radio spectrum[9] from ~ -1.0 to ~ -1.6 at $\nu > 2.5$ GHz (Stroe et al. 2016), in contrast with the simple picture of a single power-law spectrum predicted from the standard acceleration model (i.e., diffusive shock acceleration (DSA); Enßlin et al. 1998). Possible explanations were given by Kang & Ryu (2016), who suggested a model where a shock passed through a region containing fossil

[8] Clay Fellow.

[9] The radio spectrum is defined as $S_\nu \propto \nu^\alpha$, with α the spectral index.

Table 1
Datacube Information

uv-taper (arcsec)	Weighting	Robust	Resolution (arcsec × arcsec)	No. Channels		$\Delta\nu$ (MHz)		$\sigma_{\rm rms[1.26-3.60GHz]}$ (μJy beam^{-1})		
				1–2 GHz	2–4 GHz	1–2 GHz	2–4 GHz	*I*	*Q*	*U*
2.5	uniform	N/A	2.7 × 2.7	104	75	4	16	**12.1**	**11.2**	**11.3**
2.5	Briggs	0	4.55 × 4.55	104	75	4	16	**8.9**	**10.1**	**10.0**
5	Briggs	0	7 × 7	104	136	4	8	7.9	5.1	5.2
10	Briggs	0	13 × 13	104	136	4	8	18.2	5.1	5.4

Note. Column (4): final resolution of the data cubes. Columns (5) and (6): total number of channels in the 1–2 GHz and 2–4 GHz bands. Columns (7) and (8): channel width in MHz in the 1–2 GHz and 2–4 GHz bands. Columns (9)–(11): noise map for the Stokes *I*, *Q*, and *U* data cubes. The noise levels in the last column have been calculated as the standard deviation of the datacube, in a central, "empty" region of the cluster. For the 2.″5-tapered images, we only produced stamps of the single sources; hence, we report the map noise locally to RN.
Columns (1)–(3): Gaussian *uv*-taper, weighting, and robust parameters for the imaging

electrons, by Donnert et al. (2016), who suggested the presence of exponential magnetic field amplification in the downstream region (with the shock being located at the outermost edge of the relic), and by Basu et al. (2016), who proposed a nonnegligible contribution from the Sunyaev–Zel'dovich (SZ) effect (also supported by single-dish observations; see Loi et al. 2017). Single-dish observations revealed that this relic is strongly polarized (up to 60% at 8.35 GHz; Kierdorf et al. 2017), although the poor resolution (i.e., 90″) strongly limited their analysis. From the relic width (55 kpc) and X-ray downstream velocity (about 1000 km s^{-1}), van Weeren et al. (2010) estimated magnetic field strengths of 5 or 1.2 μG.

The paper is organized as follows: In Section 2 we describe the data reduction and the imaging procedures. In Section 3 we present the *QU*-fitting approach. We highlight the effect of the Galactic rotation measure (RM) in Section 4. The results and discussion are given in Sections 5 and 6. We end with the conclusion in Section 7. Throughout the paper, we assume a flat ΛCDM cosmology with $H_0 = 70$ km s^{-1} Mpc^{-1}, $\Omega_{\rm m} = 0.3$, and $\Omega_\Lambda = 0.7$, which gives a conversion factor of 3.22 kpc arcsec^{-1} and a luminosity distance of ≈ 944 Mpc, at the cluster's redshift ($z = 0.192$; Kocevski et al. 2007).

2. Observations and Data Reduction

We made use of the same 1–4 GHz VLA observations presented in Di Gennaro et al. (2018), to which we refer for a detailed description of the data reduction. The observations were made with all four array configurations (namely, A, B, C, and D), some of them split into sub–data sets (see Table 1 in Di Gennaro et al. 2018). Due to the large angular size of the cluster and the limited field of view (FOV) at 2–4 GHz, we observed three separate pointings in this frequency range. We briefly summarize the data reduction strategy below.

First, we Hanning-smoothed the data and removed radio frequency interference (RFI) with the *tfcrop* mode from the `flagdata` task in `CASA`. Then, we calibrated the antenna delays, bandpass, cross-hand delays, and polarization leakage and angles using the primary calibrators 3C 138, 3C 147, and/or 3C 48. For the polarization leakage calibration, we can only make use of an unpolarized source;[10] hence, we discarded all the sub–data sets where 3C 48 was the only calibrator (for further details, see Di Gennaro et al. 2018). We determined the global cross-hand delay solutions (`gaintype='KCROSS'`) from the polarized calibrator 3C 138, taking an RL-phase difference of −10° (both L and S band) and polarization fractions of 7.5% and 10.7% (L and S band, respectively). We used 3C 147 to calibrate the polarization leakage terms (`poltype='Df'`) and 3C 138 to calibrate the polarization angle (`poltype='Xf'`). The solution tables were applied on the fly to determine the complex gain solution for the secondary calibrator J2202 +4216. Additional RFI removal was performed, using the *tfcrop* and *rflag* modes (in `CASA`) and `AOFlagger` (Offringa et al. 2010), before and after applying the calibration tables to the target field, respectively. The data were averaged by a factor of two in time and a factor of four in frequency. This reflects a frequency resolution (i.e., channel width) of $\Delta\nu = 4$ MHz and $\Delta\nu = 8$ MHz at 1–2 GHz and 2–4 GHz, respectively. The only exception is the 2.″5-tapered data set at 2–4 GHz, for which we average by a factor of eight, i.e., $\Delta\nu = 16$ MHz. Finally, self-calibration was performed to refine the amplitude and phase calibration on the target.

To retrieve the images for all the Stokes parameters (i.e., *I*, *Q*, and *U*) at each channel $\boldsymbol{\Delta\nu}$, as required for a detailed polarization analysis, we employed the `WSClean` (Offringa et al. 2014). Images were produced with different weightings (i.e., `Briggs` and `uniform`), and *uv*-tapers (i.e., 2.5″, 5″, and 10″). Bad spectral windows and channels were discarded from the final analysis. For the Stokes *Q* and *U* images, we also used the options `-join-channels`, `-join-polarizations`, and `-squared-channel-joining`, which prevent the *Q* and *U* flux from being averaged out to zero.[11] After imaging, channel images that were too noisy or low-quality were removed. In the end, a total of 240 channels for the 5″- and 10″-tapered images and 179 channels for the 2.″5-tapered images were used. This results in a final frequency coverage of 1.26–3.60 GHz. The single-channel images were regridded to the same pixel grid and convolved to the same resolution (see Table 1). Finally, all the single images were primary beam corrected, by taking the beam variation with the frequency taken into account,[12] and merged into a single datacube for each Stokes parameter. Errors in the single-channel images were estimated using the rms

[10] In principle, a calibrator with enough parallactic angle coverage can also be used for the leakage calibration. This kind of calibrator was not available in our observations.

[11] https://sourceforge.net/p/wsclean/wiki/RMSynthesis/

[12] The beam shapes have been obtained with `CASA` v. 5.3.

noise level from a central, empty region of the cluster (at 7″ and 13″ resolution) or locally for the sources of interest (at 4.″5 and 2.″7 resolution).

3. Polarization Theory and Modeling Approach

The linear polarization emission can be described in terms of Stokes parameters for the total intensity, I, and the orthogonal components, Q and U,

$$P(\lambda^2) = p(\lambda^2)I(\lambda^2)\exp[2i\chi(\lambda^2)] = Q(\lambda^2) + iU(\lambda^2), \quad (1)$$

and λ is the observing wavelength. Here $p(\lambda^2)$ is the fractional (or degree of) polarization and $\chi(\lambda^2)$ is the polarization angle, which are wavelength-dependent quantities that can be written as

$$p(\lambda^2) = \frac{P(\lambda^2)}{I(\lambda^2)} = \frac{\sqrt{Q^2(\lambda^2) + U^2(\lambda^2)}}{I(\lambda^2)} \quad (2)$$

and

$$\chi(\lambda^2) = \frac{1}{2}\arctan\left(\frac{U(\lambda^2)}{Q(\lambda^2)}\right). \quad (3)$$

The passage of the polarized radiation through a foreground magneto-ionic medium, such as the ICM, results in a rotation of polarization plane via the Faraday effect according to

$$\chi(\lambda^2) = \chi_0 + \mathrm{RM}\lambda^2, \quad (4)$$

where χ_0 is the intrinsic polarization angle and RM is the Faraday rotation measure. This is defined as

$$\mathrm{RM} = 0.81\int_{\mathrm{source}}^{\mathrm{observer}} n_e B_{\parallel} dl \quad [\mathrm{rad\ m^{-2}}], \quad (5)$$

where n_e is the electron density (in $\mathrm{cm^{-3}}$), $B_{\parallel}$ the magnetic field (in μG) along the line of sight, and l the path length through the magneto-ionic medium (in pc), and with the sign of the equation defined positive for a magnetic field pointing toward the observer.

The traditional way to retrieve the intrinsic polarization angle χ_0 is to observe χ at several wavelengths and linearly fit Equation (4). The long-standing problem of this approach is the lack of a sufficient number of $\chi(\lambda^2)$ measurements. In this work, this issue is overcome by the large number of channel images with high signal-to-noise ratio (S/N) of our wide-band observations (see Section 3.1).

Several models of the polarized signal, in the presence of Faraday rotation, are known. In the simplest scenario, Equation (1) can be written as

$$P(\lambda^2) = p_0 I\exp[2i(\chi_0 + \mathrm{RM}\lambda^2)], \quad (6)$$

with p_0 the intrinsic polarization fraction. This corresponds to the physical situation of a single Faraday screen in the foreground. In this case, $d\chi/d\lambda^2$ and $p(\lambda)$ are constant.

Observations have shown that radio relics depolarize at frequencies $\lesssim$1 GHz (Brentjens 2011; Pizzo et al. 2011; Ozawa et al. 2015). Common depolarization mechanisms are external and internal Faraday rotation dispersion (EFD and IFD, respectively; see Sokoloff et al. 1998, for the detailed parameterization of those mechanisms). EFD occurs when variations in the magnetic field direction are not resolved in the single beam (Burn 1966; Tribble 1991). For a Gaussian distribution of RM, the observed polarization is parameterized as

$$P(\lambda^2) = p_0 I\exp(-2\sigma_{\mathrm{RM}}^2\lambda^4)\exp[2i(\chi_0 + \mathrm{RM}\lambda^2)], \quad (7)$$

where σ_{RM} is the dispersion about the mean RM across the beam on the sky.

On the other hand, IFD occurs when the emitting source and the Faraday screen (i.e., the rotating layer) are mixed. In this case, depolarization is due to the random direction of the plane of polarization through the emitting region, and it can be parameterized as

$$P(\lambda^2) = p_0 I\left[\frac{1 - \exp(-2\varsigma_{\mathrm{RM}}^2\lambda^4)}{2\varsigma_{\mathrm{RM}}^2\lambda^4}\right]\exp[2i(\chi_0 + \mathrm{RM}\lambda^2)], \quad (8)$$

where ς_{RM} is the internal dispersion of the random field.

3.1. QU-*modeling Approach*

Stokes $Q(\lambda^2)$ and $U(\lambda^2)$ fitting has been used in the literature to determine the polarization properties of a magneto-ionic layer (e.g., O'Sullivan et al. 2012; Ozawa et al. 2015; Anderson et al. 2016). In this approach, $Q(\lambda^2)$ and $U(\lambda^2)$ were fitted simultaneously with cosine and sine models, while $I(\lambda^2)$ was fitted with a log-parabolic model (see also Massaro et al. 2004), which represents a curved spectrum, as suggested by Stroe et al. (2016) and given the large bandwidth used:

$$I_\nu = I_0\nu^{a+b\log(\nu/\nu_{\mathrm{ref}})}, \quad (9)$$

where we fixed the reference frequency ν_{ref} to 1 GHz.

In this model, b is the curvature parameter and the spectral index is calculated as the log-derivative, i.e., $\alpha = a + 2b\log(\nu/\nu_{\mathrm{ref}})$. For each channel image in the $I(\lambda^2)$, $Q(\lambda^2)$, and $U(\lambda^2)$ data cubes, the uncertainties were computed by adding in quadrature the relative (spatial) map noise and 5% of the Stokes I, Q, and U flux in each channel. Here the 5% represents a spatially independent intrinsic scatter that takes into account the flux variations between the single-frequency channel maps. The origin of this scatter is not fully clear, but it is probably related to bandpass calibration and/or deconvolution uncertainties.

We fitted our data with the Markov Chain Monte Carlo (MCMC) method[13] (Foreman-Mackey et al. 2013) to explore the best set of model parameters (Ozawa et al. 2015). During the fitting procedure, all the parameters (i.e., I_0, a, and b for Stokes I, and p_0, χ_0, RM, and σ_{RM}^2 for the combined Stokes Q and U) were left free to vary through the full parameter space. In the fitting, we constrained p_0, χ_0, and σ_{RM}^2 (or $\varsigma_{\mathrm{RM}}^2$) to the physical conditions

$$\begin{cases} 0 \leqslant p_0 \leqslant 1 \\ 0 \leqslant \chi_0 < \pi \\ \sigma_{\mathrm{RM}}^2 \geqslant 0 \text{ or } \varsigma_{\mathrm{RM}}^2 \geqslant 0, \end{cases} \quad (10)$$

and we assumed a single-RM component model (see also Appendix A)). The upper limit for the polarization angle is set to π because the polarization vectors have no preferred direction. In this convention, $\chi_0 = 0$ and $\chi_0 = \pi/2$ give the north/south and east/west directions, respectively. We chose

[13] The initial guesses for the parameters were obtained with the least-squares method (*scipy.optimize.leastsq* in Python).

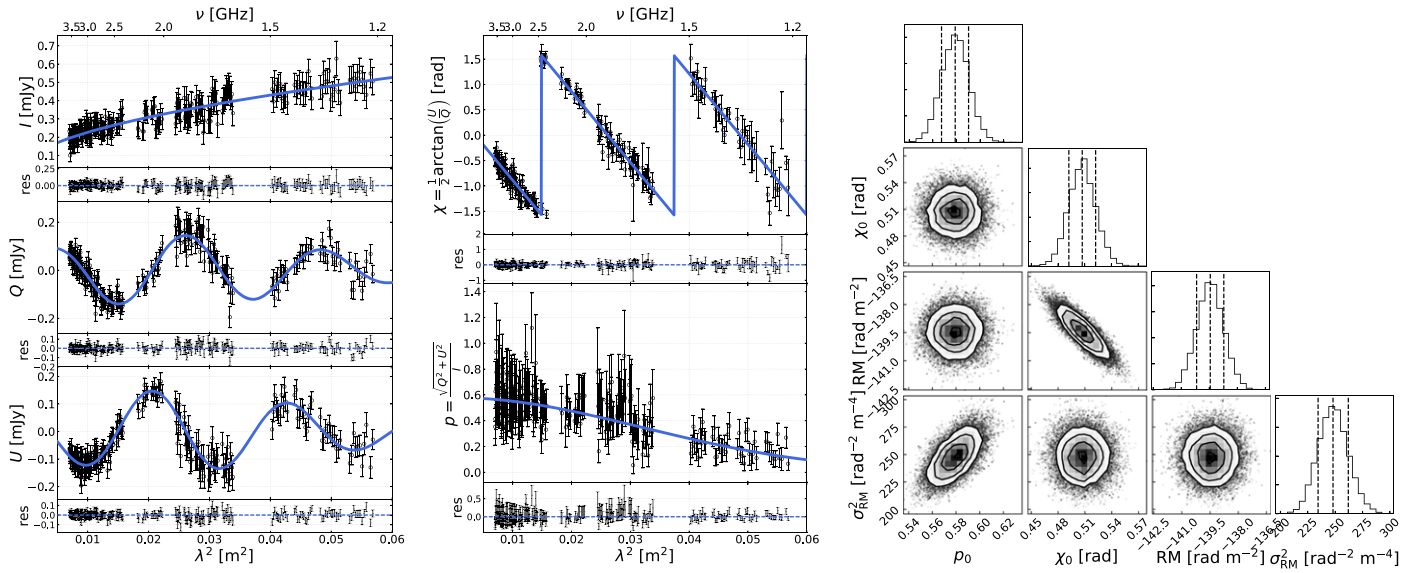

Figure 1. Result of the *QU*-fit assuming the external depolarization model (EDF; Equation (7)) on a single pixel of the northern relic. Left panel: fits on Stokes *I*, *Q*, and *U* fluxes. Middle panel: resulting fractional polarization, $p(\lambda^2)$, and polarization angle, $\chi(\lambda^2)$, estimated from Equations (2) and (3), respectively. Right panel: corner plot for the distribution of the uncertainties in the fitted polarization parameters (i.e., p_0, χ_0, RM, and $\sigma^2_{\rm RM}$); contour levels are drawn at [0.5, 1.0, 1.5, 2.0]σ, with σ the 68% statistical uncertainty (see dashed lines in the 1D histogram).

to include depolarization in our fit, as our observations showed a decrease in polarization fraction toward longer λ^2. It is worth noting that the p_0 value obtained from the MCMC fit could be an underestimation of the intrinsic polarization fraction, because of the limited λ^2 coverage and possible misalignment of the intrinsic polarization angle χ_0 from different emitting sites along the line of sight. Hereafter we refer to p_0 as the best-fit intrinsic polarization fraction. The uncertainties on the best-fitting parameters were determined with the MCMC analysis. The results of the fitting procedure using the EFD model on a representative single pixel in the cluster northern relic are displayed in Figure 1. Similar results were found using the IDF model (Equation (8)), except for $\varsigma_{\rm RM}$, which is higher owing to the different functional way it describes the depolarization.

4. Rotation Measure from Our Galaxy

The best-fit RM value obtained could, in principle, give information on the magnetic field structure of the diffuse radio emission in the cluster (Equation (5)). However, in order to have a reliable estimation of the RM associated with the ICM, the contribution of the foreground Galactic RM needs to be estimated and removed from the calculations.

The Galactic coordinates of CIZAJ2242 are $l = 104°$ and $b = -5°$, meaning that the cluster lies close to the Galactic plane. Hence, the RMs of the cluster sources are strongly affected by the Faraday rotation from our Galaxy. Using the map of the Galactic contribution to Faraday rotation provided by Oppermann et al. (2015),[14] we found an average contribution of about $-65 \pm 57\,{\rm rad\,m^{-2}}$ in a region of 20′ around the cluster center coordinates. However, the current available Galactic RM map is affected by very poor angular resolution (i.e., ∼10′ pixel^{-1}), which is comparable with the cluster size (∼15′). For this reason, we lack detailed information on the RM variations on the cluster/subcluster scale.

We investigated the RM values of compact sources within the FOV of our observations but outside the cluster region. In this way, we exclude the contribution of the ICM on the RM estimation. Since the size of the primary beam depends on the frequency as FOV $\propto \nu^{-1}$, and we want to maximize the area where we search for polarized sources, we only used the 1–2 GHz observations. We found a total of 10 sources in the 1–2 GHz FOV (∼18′; see Figure 2). Their RM values, listed in Table 2, are consistent with the average Galactic RM value found by Oppermann et al. (2015), with a median value of about $-80\,{\rm rad\,m^{-2}}$ and a standard deviation of about $42\,{\rm rad\,m^{-2}}$. Moreover, we found that sources close to each other (i.e., sources 4 and 5, and sources 7 and 10) have similar RM, suggesting that the Galactic foreground might remain approximately constant in that region, on those spatial scales (**3′–5′**, i.e., few hundreds of kiloparsecs, at the cluster distance). However, we find a strong variation from RM north to south and east to west, although without a clear trend. It remains therefore difficult to quantify a unique RM value from the Galactic foreground and to subtract it from our measured RM values for the cluster sources. For this reason, in the following maps and plots we report the best-fit RM value, including the Galactic contribution.

5. Results

5.1. Polarized Flux Densities and Fractions

We obtained the total averaged polarization images in the 1.26–3.60 GHz band by means of the RM-Synthesis technique (Brentjens & de Bruyn 2005), using the `pyrmsynth` tool[15]. In Figure 3 and in the top panel of Figure 4 we show the total averaged polarization images of the entire cluster at 7″ resolution and of the northern relic at 2.″7 resolution, at the effective frequencies of 2.3 and 2.0 GHz, respectively. We retrieve the polarized intensity at the canonical frequencies, i.e., 1.5 and 3.0 GHz (i.e., at wavelengths of 0.2 and 0.1 m, respectively),

[14] https://wwwmpa.mpa-garching.mpg.de/ift/faraday/2014/index.html

[15] https://github.com/mrbell/pyrmsynth

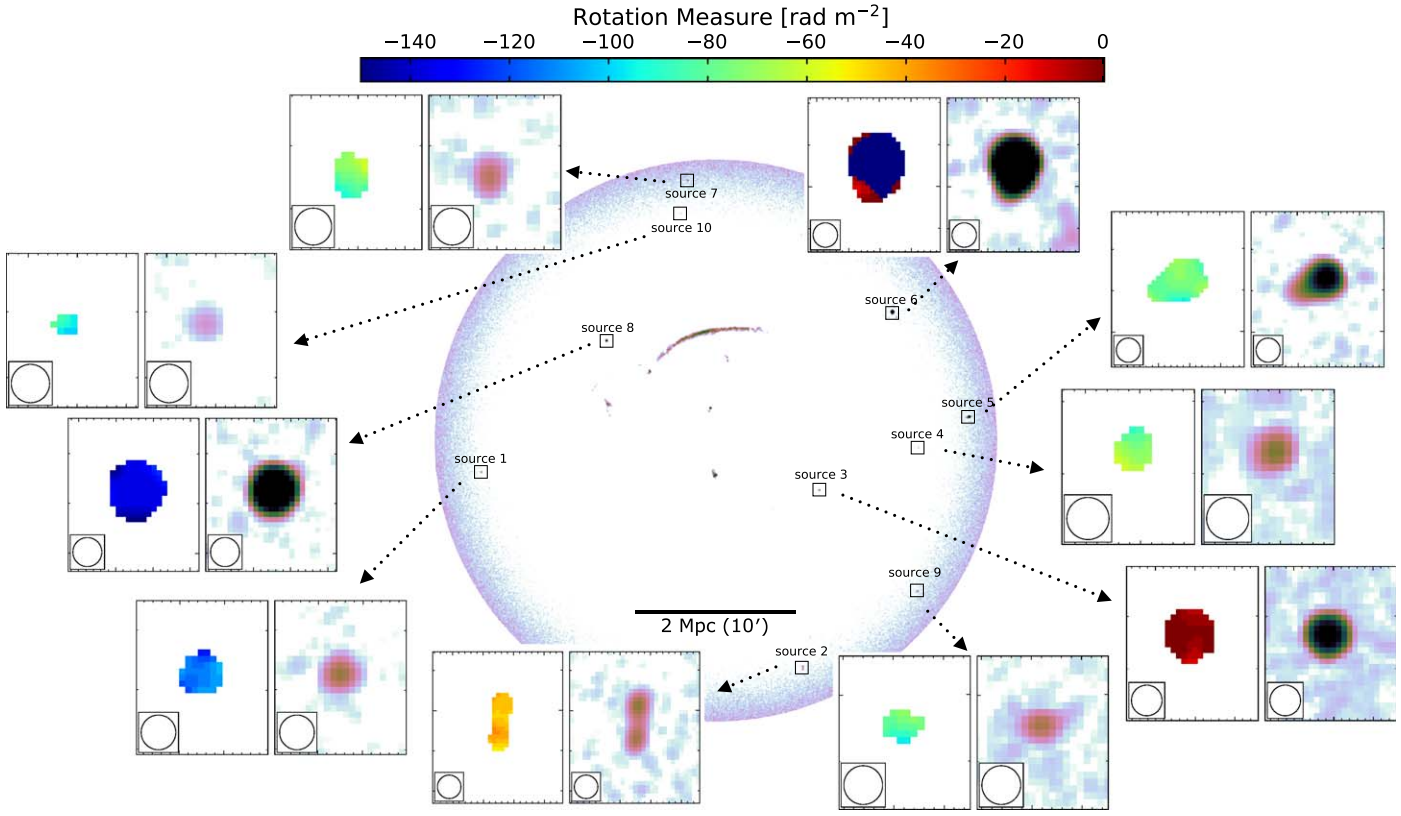

Figure 2. Total polarized emission of the 1–2 GHz FOV (FOV $\sim$ 18′ in radius) to search for polarized radio galaxies outside CIZAJ2242. A zoom-in of those sources is shown in the insets, where the RM and the total intensity are displayed in the left and right panels, respectively. The RM color scale is fixed for all the sources. The averaged RM values of those sources are listed in Table 2.

Table 2
Averaged RM Values of the Sources Labeled in Figure 2 Observed in the 1–2 GHz Frequency Range

Source	R. A. J2000 (^{h} ^{m} ^{s})	Decl. J2000 ($^{\circ}$ $'$ $''$)	$\langle$RM$\rangle \pm$ std(RM) (rad m^{-2})
1	22 44 31.5	+53 00 39.0	-113.0 ± 5.4
2	22 42 12.4	+52 47 56.5	-43.9 ± 3.6
3	22 42 05.2	+52 59 32.0	$+1.2 \pm 8.1$
4	22 41 22.1	+53 02 15.5	-71.7 ± 7.2
5	22 41 00.1	+53 04 15.7	-77.4 ± 5.1
6	22 41 33.1	+53 11 07.7	-155.9 ± 1.4
7	22 43 02.2	+53 19 42.2	-76.0 ± 8.5
8	22 43 37.5	+53 09 15.5	-137.2 ± 5.0
9	22 41 22.9	+52 52 54.3	-81.1 ± 6.7
10	22 43 05.2	+53 17 33.8	-92.0 ± 6.4

Note. The "uncertainty" on RM is represented by the standard deviation of the RM pixel distribution within the source. Source 3 and source 8 are labeled as sources A and N in Figure 3, respectively.

using the fit results of Equation (7) as described in Section 3.1. In Table 3 we report the polarized and total flux densities, the corresponding factional polarization (Equation (3)), and the amount of depolarization $\mathrm{DP}^{3.0\mathrm{GHz}}_{1.5\mathrm{GHz}} = 1 - (p_{1.5\mathrm{GHz}}/p_{3.0\mathrm{GHz}})$[16], for the diffuse radio sources in the cluster.

We detect significant polarized emission both from the numerous radio galaxies and from the diffuse radio sources. The brightest polarized structure of the cluster is the northern relic (RN), with integrated polarized flux densities of $P_{3.0\mathrm{GHz}} = 17.0 \pm 0.9$ and $P_{1.5\mathrm{GHz}} = 19.4 \pm 1.0$ mJy (Table 3). The relic presents a similar continuous shape to that detected in total intensity emission (see radio contours in Figure 3). At 2.″7 resolution (i.e., the highest resolution available in our observations), the polarized emission traces the relic's filamentary structure observed already in the total intensity (see top panel of Figure 4 in this manuscript and Figure 7 in Di Gennaro et al. 2018). Hints of polarized emission at 13″ resolution are seen also from the very faint relic northward of RN, i.e., R5, with a high degree of polarization at both 3.0 and 1.5 GHz (i.e., about 35% and 30%).

Particularly bright in polarization is also the relic located eastward of RN, i.e., R1 ($P_{3.0\mathrm{GHz}} = 1.5 \pm 0.1$ and $P_{1.5\ \mathrm{GHz}} = 2.6 \pm 0.1$ mJy). The relic labeled as R4 shows a particularly high degree of polarization at both 3.0 and 1.5 GHz ($\sim$50%), with negligible wavelength-dependent depolarization. On the contrary, the relic westward of RN, i.e., R3, undergoes strong depolarization from 3.0 to 1.5 GHz ($\mathrm{DP}^{3.0\mathrm{GHz}}_{1.5\mathrm{GHz}} \sim 80\%$).

Faint polarized emission is observed in the southern relic (RS), at 13″ resolution. Here the emission only comes from two out of the five "arms" that were detected in Di Gennaro et al. (2018), i.e., only RS1 and RS2. This is not completely a surprise, as these two "arms" are also the brightest in total intensity (see Di Gennaro et al. 2018).

No polarized emission is detected for the diffuse sources R2 and I. Finally, we detect polarized emission from the radio galaxies in and around the cluster (i.e., A, B, C, D, E, F, H, J, K1, M, N, and O), whose degree of polarization at 1.5 and 3.0 GHz ranges between 1% and 10%, consistently with other similar objects (e.g., O'Sullivan et al. 2012).

[16] In this convention, $\mathrm{DP}^{3.0\mathrm{GHz}}_{1.5\mathrm{GHz}} = 0$, i.e., $p_{1.5\mathrm{GHz}} = p_{3.0\mathrm{GHz}}$, means no depolarization, while $\mathrm{DP}^{3.0\mathrm{GHz}}_{1.5\mathrm{GHz}} = 1$, i.e., $p_{1.5\mathrm{GHz}} \sim 0$, means full depolarization.

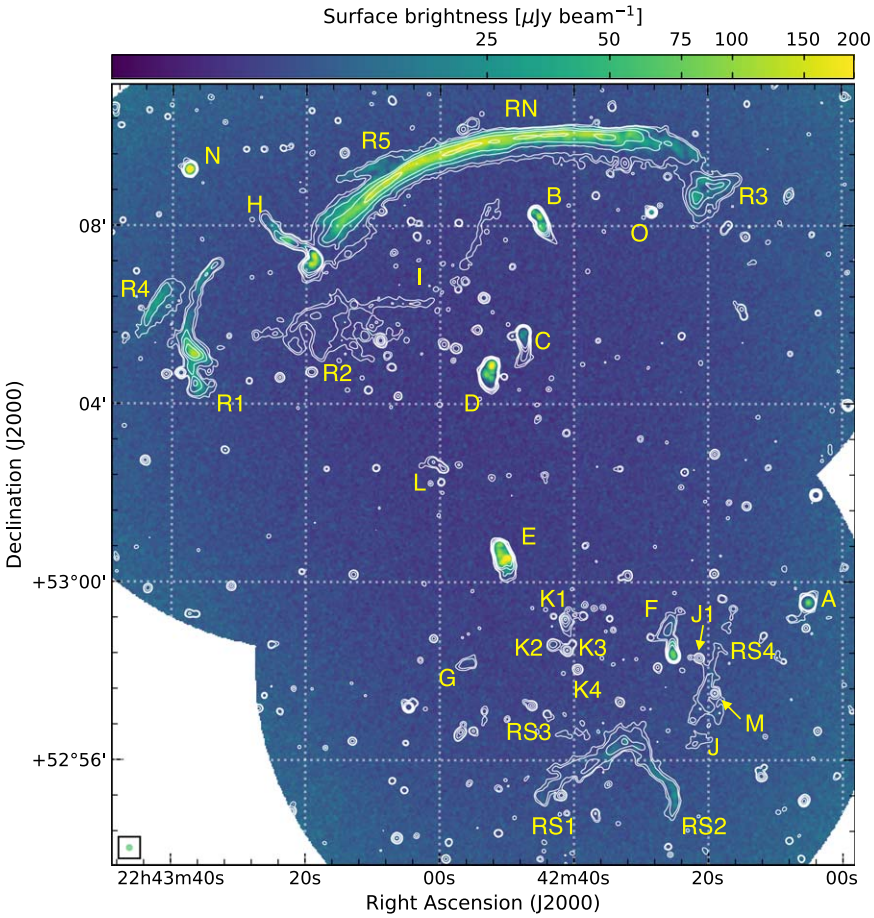

Figure 3. Total averaged polarized emission for CIZAJ2242 in the 1.26–3.60 GHz band (effective frequency of 2.3 GHz) at 7″ resolution. This image is not corrected for the Ricean bias. The radio contours are from the averaged total intensity image, in the same frequency band and at the same resolution, with contours drawn at levels of $3\sigma_{\rm rms} \times \sqrt{[1, 4, 16, 64, 256,\ldots]}$, with $\sigma_{\rm rms} = 4.2\ \mu$ Jy beam^{-1}. Sources are labeled following Figure 2 in Di Gennaro et al. (2018).

5.2. Intrinsic Fractional Polarization, Intrinsic Polarization Angle, RM, and Depolarization Maps

In Figure 5 we show a comparison between the total intensity and total averaged polarization maps of the northern relic at 7″ resolution (panels (a) and (b), respectively), best-fit intrinsic and 1.5 GHz polarization fractions (p_0 and $p_{1.5\rm GHz}$, panels (c) and (d), respectively), and RM (panel (e)) and external wavelength-dependent depolarization ($\sigma_{\rm RM}$; panel (f)) maps. The polarization best-fit parameter maps of the full cluster at 13″ resolution are shown in Figure 6. These result from the *QU*-fitting approach for the case of the external depolarization (Equation (7)) for each pixel with averaged polarized emission above $f \times \sigma_{{\rm rms},P}$. Here $\sigma_{{\rm rms},P}$ is obtained at the given resolution as the rms level of the averaged polarized emission measured in a central, "empty" region of the cluster. We use $f = 2$ for the 2.″5-tapered images with `weighting='uniform'` and $f = 3$ for all the other resolutions and `weighting='Briggs'`. The corresponding uncertainty maps are displayed in Appendix B.

The northern relic (RN) shows very high best-fit intrinsic polarization fraction values at the outermost edge, with the eastern side up to 60% and the western side up to 40% polarized. We also note a radial decreasing of p_0 toward the cluster center. The intrinsic polarization angles approximately follow the shock normal, which is assumed to be perpendicular to the Stokes *I* edge, supporting the scenario where the magnetic field is aligned after the shock passage (see also bottom panel of Figure 4). The angles remain aligned also in the downstream region. The RM value is not constant along the relic; it spans east to west from RM ~ -150 to ~ -130 rad m^{-2}, respectively, with a median value of about -141 rad m^{-2}. Given the large distance from the cluster center (i.e., $\sim$1.5 Mpc), where the contribution of the ICM is likely low, we suggest that this median value is mostly associated with the Galactic foreground (see Section 4). The variations in RM across the northern relic ($\sim$30 rad m^{-2}) have a dominant scale of $\sim$15″–30″, and we cannot distinguish, with the available data, whether this is due to fluctuations in our Galaxy or fluctuations in the ICM (see Section 6.5). Similar east–west RM and p_0 variations were reported with Effelsberg observations at 4.85 and 8.35 GHz (Kierdorf et al. 2017). To the contrary, the RM value measured on the western side of the relic (RM ~ -130 rad m^{-2}) differs from what has been found by the Sardina Radio Telescope at 6.6 GHz (RM ~ -400 rad m^{-2}; Loi et al. 2017). No north–south best-fit intrinsic polarization gradient across the relic's width was found by either Kierdorf et al. (2017) or Loi et al. (2017), although their observations suffer from much lower resolution (i.e., 90″ and 2.′9, respectively), which smoothed out any possible downstream gradient. Interestingly, we measure RM values of about -100 rad m^{-2} where the relic breaks in the RN1–RN2 and RN3–RN4 filaments (see panel (e) of Figure 5). Finally, we do not find any particular east–west trend in the $\sigma_{\rm RM}$ behavior, with an overall value of $\sigma_{\rm RM} \sim$ 15–20 rad m^{-2} (see panel (f) of

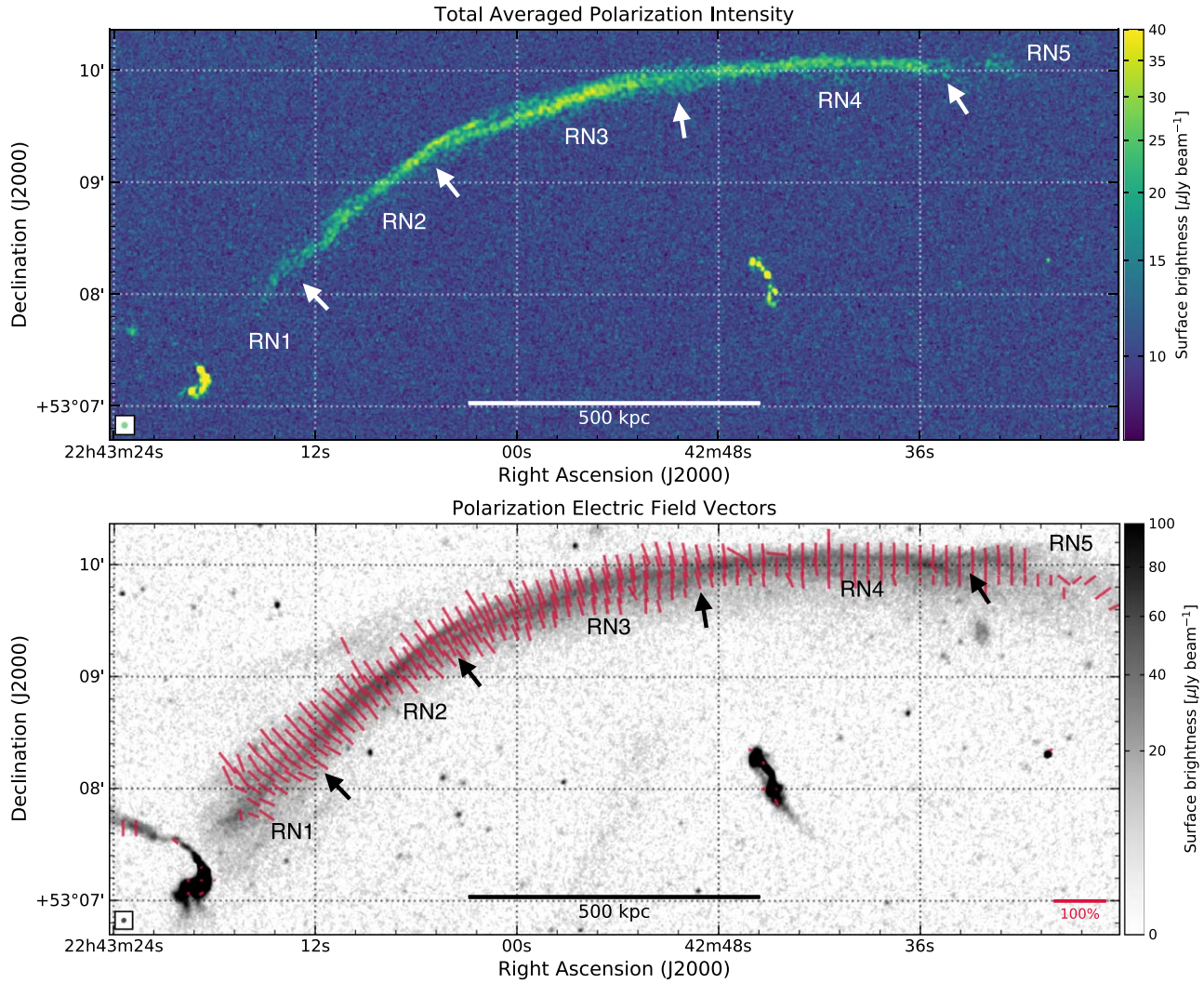

Figure 4. Top panel: high-resolution ($2\farcs7 \times 2\farcs7$) total averaged polarized image in the 1.26–3.60 GHz band (effective frequency of 2.0 GHz) zoomed in on the northern relic ($\sigma_{Q,\mathrm{rms}[1.26-3.60\ \mathrm{GHz}]} = 11.2$ and $\sigma_{U,\mathrm{rms}[1.26-3.60\ \mathrm{GHz}]} = 11.3$ μJy beam^{-1}). As for Figure 3, this image is not corrected for the Ricean bias. Bottom panel: high-resolution ($2\farcs1 \times 1\farcs8$) Stokes I observation in the 1–2 GHz band (Di Gennaro et al. 2018) with the polarization electric field vectors at $2\farcs7$ resolution, corrected for Faraday rotation, displayed in red; the length of the vectors is proportional to the intrinsic polarization fraction (scale in the lower right corner). White and black arrows in the two panels indicate the points where the relic breaks into separate filaments, following Figure 7 in Di Gennaro et al. (2018).

Table 3
Polarized (P_ν) and Total Intensity (I_ν) Flux Densities and Integrated Polarization Fraction (p_ν) for the Diffuse Radio Sources Labeled in Figure 3 at $\nu = 1.5$ and 3.0 GHz

Source	Resolution (arcsec × arcsec)	$P_{3.0\mathrm{GHz}}$[a] (mJy)	$I_{3.0\mathrm{GHz}}$ (mJy)	[b] $p_{3.0\mathrm{GHz}}$	$P_{1.5\mathrm{GHz}}$[a] (mJy)	$I_{1.5\mathrm{GHz}}$ (mJy)	$p_{1.5\mathrm{GHz}}$[a]	$\mathrm{DP}^{3.0\mathrm{GHz}}_{1.5\mathrm{GHz}}$
RN	7 × 7	17.0 ± 0.9	45.5 ± 2.3	0.37	19.4 ± 1.0	105.2 ± 5.3	0.18	0.51
RS1+RS2	13 × 13	1.2 ± 0.1	5.7 ± 0.3	0.22	2.3 ± 0.1	11.2 ± 0.6	0.20	0.06
R1	7 × 7	1.5 ± 0.1	6.4 ± 0.3	0.28	2.6 ± 0.1	13.2 ± 0.7	0.19	0.15
R2	13 × 13	…	3.7 ± 0.2	…	…	7.6 ± 0.4	…	…
R3	7 × 7	0.9 ± 0.05	3.9 ± 0.2	0.23	0.5 ± 0.02	10.1 ± 0.5	0.05	0.77
R4	7 × 7	0.7 ± 0.04	1.5 ± 0.1	0.47	1.5 ± 0.1	3.4 ± 0.2	0.46	0.03
R5	13 × 13	0.5 ± 0.03	1.5 ± 0.1	0.35	1.0 ± 0.1	3.2 ± 0.2	0.31	0.12
I	13 × 13	…	1.6 ± 0.2	…	…	3.5 ± 0.3	…	…

Notes. The depolarization fraction between the two frequencies is shown in the last column.

[a] Uncertainties are of the same order as those on the total intensity, which are given by $\sqrt{(\zeta I_\lambda)^2 + \sigma^2_{\mathrm{rms},I} N_{\mathrm{beam}}}$ ($\zeta = 0.05$ is the calibration uncertainty, $\sigma_{\mathrm{rms},I}$ is the Stokes I noise map, and $N_{\mathrm{beam}} = A_{\mathrm{source}}/A_{\mathrm{beam}}$ is the number of beams in the source where we measure the flux).

[b] Uncertainties are dominated by the precision on the leakage calibration (0.5%; https://science.nrao.edu/facilities/vla/docs/manuals/obsguide/modes/pol).

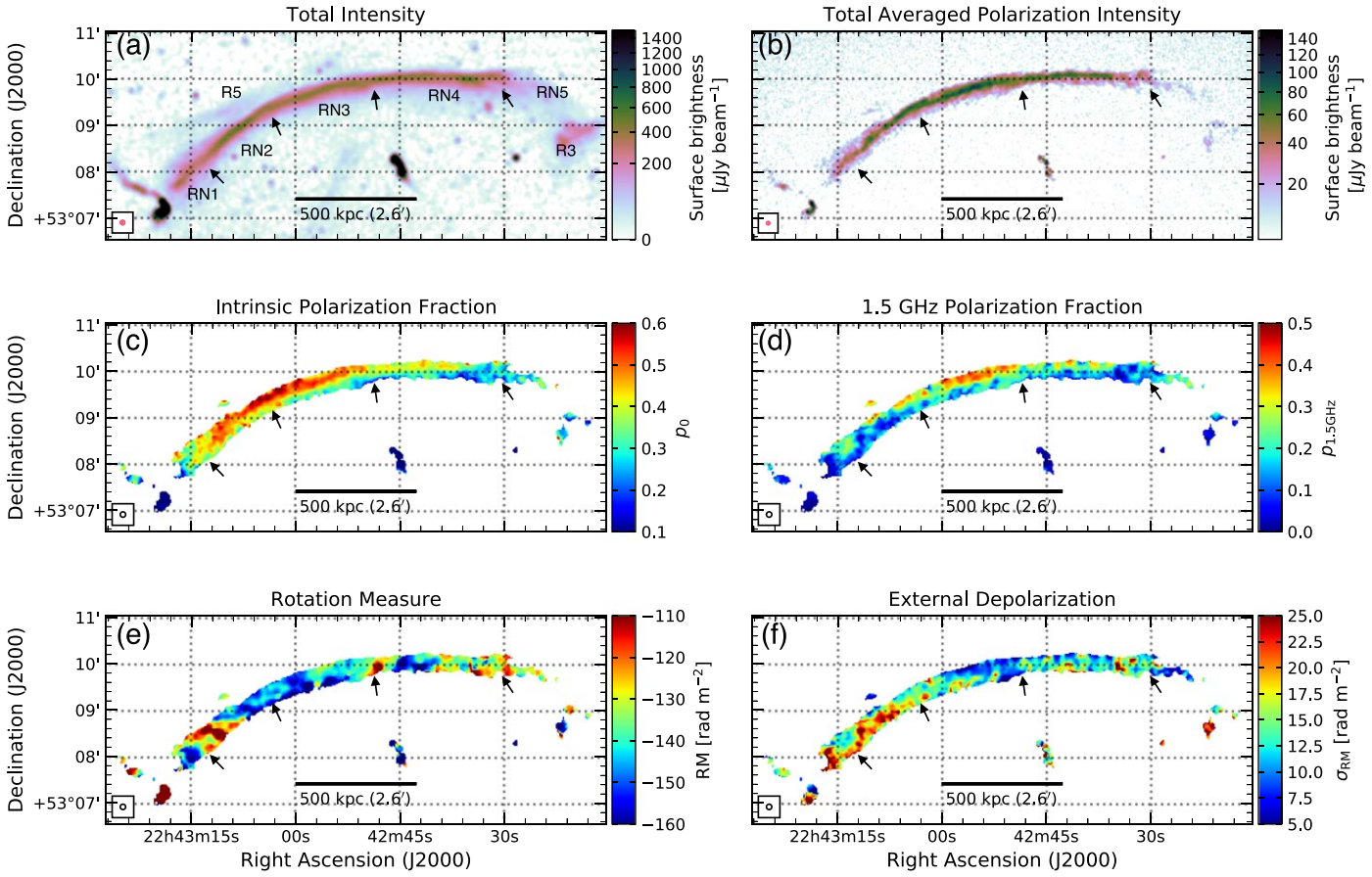

Figure 5. (a, b) The 1–4 GHz Stokes *I* emission of the northern relic (Di Gennaro et al. 2018) and corresponding 1.26–3.60 GHz averaged polarized emission (not corrected for the Ricean bias) at $\sim 5''$ resolution. (c–f) Intrinsic polarization fraction, polarization fraction at 1.5 GHz, and RM and external depolarization maps at $7''$ resolution. Black arrows in the plots are located at the same physical coordinates and indicate the points where the relic breaks into separate filaments (see also Figure 4 in this manuscript and Figure 7 in Di Gennaro et al. 2018). Uncertainty maps corresponding to panels (c)–(f) are displayed in Appendix B.

Figure 5). These values differ from the high-frequency observations, as Kierdorf et al. (2017) did not measure any depolarization for the northern relic.

The radio relic R4 is characterized by a very high best-fit intrinsic polarization fraction (∼55%), while it is lower for R1, R3, and R5 (∼20%). No clear gradients have been observed for these sources, except for R3, which shows hints of increasing values of p_0 toward the cluster center. The RM values are rather constant across R1 and R4, RM ~ -142 rad m^{-2}, consistent with the one found for source N: since this radio galaxy is located outside of the cluster, its RM is likely associated with the screen of our Galaxy rather than the ICM. Also, R1 and R4 have very small values of $\sigma_{\rm RM}$, again consistent with their spatial position in the cluster, in a region of low ICM density.

In the southern relic (RS), we measure a relatively low best-fit intrinsic polarization fraction of $\sim 10\%$–25%. Across RS1 and RS2, the RM spans from ~ -90 to ~ -80 rad m^{-2}. As for the northern relic, since RS is located in the cluster outskirts, we speculate that most of its RM is due to the Galaxy. The discrepancy between RM$_{RN}$ and RM$_{RS}$ can be due to either our Galaxy, whose RM variation is very uncertain (Section 4), or to a different combination of $n_e B_{\parallel}$ along the line of sight northward and southward of the cluster ICM (see Equation (5)).

Finally, the polarized radio galaxies in the cluster field present different values of RM. This possibly reflects the combination of their different position in the ICM with the Galactic contribution, although their intrinsic RM cannot be fully excluded. Among them, sources D and C are particularly interesting. They are located, in projection, in the cluster center, and we measure a large difference in RM in the source's lobes, with the northwestern being negative (i.e., ~ -600 and ~ -200 rad m^{-2} for sources D and C. respectively) and the southeastern being positive (i.e., $\sim +300$ and $\sim +250$ rad m^{-2} for sources D and C, respectively). Such an extreme variation of RM in the lobes of the two radio galaxies probably originates in the radio galaxies themselves, although some effects might also be associated with the large amount of ICM traversed by the polarized emission. However, for these sources we find that a single-RM model does not properly fit the data, even within a single resolution element (i.e., a single pixel; see Appendix A). We therefore suggest the presence of a complex RM structure, as is observed also in other radio galaxies (e.g., O'Sullivan et al. 2012). This study is, however, beyond the scope of this paper.

6. Discussion

Radio relics are thought to trace merger-induced shock waves that (re)accelerate electrons and compress and amplify the cluster magnetic fields (e.g., Enßlin et al. 1998). While several studies have been performed to investigate the mechanism to produce the highly relativistic electrons in radio relics (e.g., Brunetti & Jones 2014; Fujita et al. 2015; Donnert et al. 2016; Kang et al. 2017), studies of their magnetic field properties have been

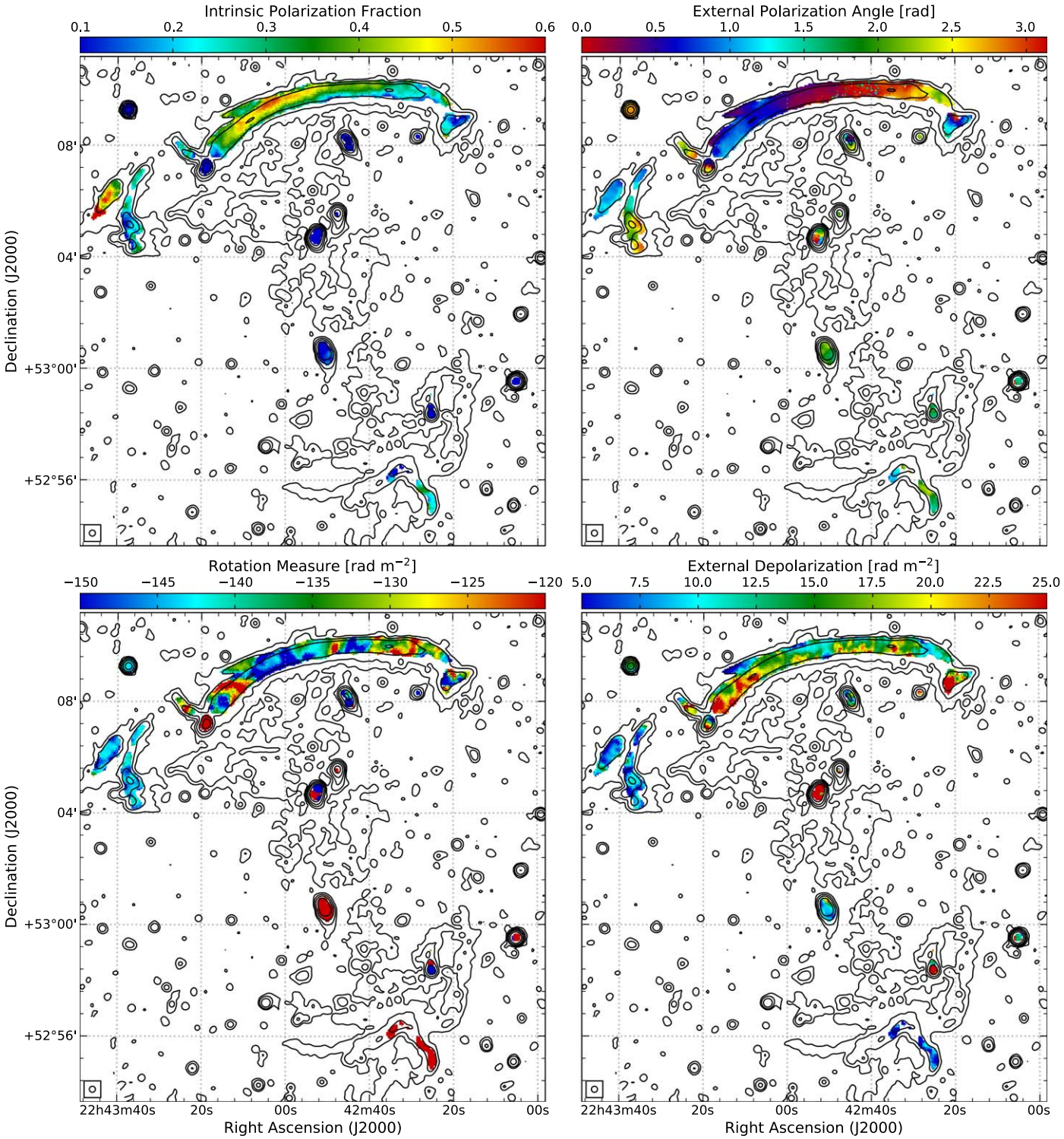

Figure 6. From top left to bottom right: intrinsic polarization fraction (p_0), intrinsic angle (χ_0), and RM and depolarization ($\sigma_{\rm RM}$) maps of CIZAJ2242 at 13″ resolution. Stokes I radio contours at the same resolution are drawn in black at levels of $3\sigma_{\rm rms} \times \sqrt{[1, 4, 16, 64, 256, \ldots]}$, with $\sigma_{\rm rms} = 6.2$ μJy beam^{-1} (Di Gennaro et al. 2018). Negative and positive uncertainty maps are displayed in Appendix B.

challenging, mostly because depolarization effects are stronger at low frequencies (i.e., $\lesssim$1 GHz).

The northern radio relic in CIZAJ2242, i.e., the Sausage relic, is well known to be highly polarized; hence, it represents one of the best targets for detailed polarization studies. Here we present the first analysis of the radial and longitudinal polarization properties of the relic in the post-shock region on tens-of-kiloparsec scales (i.e., ∼8–40 kpc). Additionally, we investigate possible correlations between the polarization parameters and look for the presence of possible underlying trends among them by calculating the running median along the x-axis, with moving boxes of 20 windows. The uncertainties are calculated as $\sigma_{\pm}/\sqrt{N}$, with $\sigma_{+} = y_{0.50} - y_{0.16}$ and $\sigma_{-} = y_{0.84} - y_{0.50}$ (with $y_{0.16}$, $y_{0.50}$, and $y_{0.84}$ representing 16%, 50% (i.e., the median), and 84% of the

distribution, respectively), and where N is the number of windows (Lamee et al. 2016). The existence of a correlation was then evaluated by means of the Pearson coefficient, r_p (Pearson 1895), where we define $|r_p| \leqslant 0.3$ as no/very weak correlation, $0.3 < |r_p| \leqslant 0.7$ as weak/moderate correlation, and $|r_p| > 0.7$ as strong correlation. We also report the Spearman coefficient, r_s, which assesses whether the relationship is monotonic (i.e., $|r_s| \leqslant 0.3$: no/very weakly monotonic; $0.3 < |r_s| \leqslant 0.7$: weakly/moderately monotonic; $|r_s| > 0.7$: strongly monotonic).

The following discussion is focused on the Sausage relic. In Section 6.1 we present the radial profiles of the best-fit polarization parameters. In Section 6.2 we discuss a possible explanation for the profile found for the best-fit p_0. In Section 6.3 we look at the contribution of the turbulent magnetic field in the post-shock region. In Section 6.4 we investigate the limitation of the observing bandwidth coverage. Finally, in Section 6.5 we look at the RM fluctuation in the relic.

6.1. Polarization Parameter Radial Profiles

We repeated the *QU*-fit using Equation (7) in beam-sized boxes (i.e., 7″, resulting in a linear size of about 20 kpc at the cluster redshift; see legend in Figures 7 and 8, and Figure C1) covering the filament RN3, which we consider to be a representative part of the relic (see Figure 5). For each single radial annulus (i.e., same-colored markers in Figures 7 and 8), the polarization parameters have a similar trend along the filament (i.e., east to west; Figure 7), with the exception of the RM, which shows a variation of about 30 rad m^{-2}. On the other hand, a clear north–south trend is visible for the best-fit intrinsic polarization fraction. It drops about 35%–40%, from an average value of $\langle p_0 \rangle_{d=0\mathrm{kpc}} = 0.40 \pm 0.04$ at the shock position to $\langle p_0 \rangle_{d=66\mathrm{kpc}} = 0.28 \pm 0.06$ in the innermost downstream annulus (top panel of Figure 7). The same trend is also observed for the polarization fraction at 1.5 GHz (Figure 8). At this wavelength, the drop is even larger, about 60% (from $\langle p_{1.5\ \mathrm{GHz}} \rangle_{d=0\mathrm{kpc}} = 0.35 \pm 0.04$ to $\langle p_{1.5\ \mathrm{GHz}} \rangle_{d=66\mathrm{kpc}} = 0.24 \pm 0.09$). A similar but opposite trend is observed for the external wavelength-dependent depolarization: here we found higher values toward the downstream region (from $\langle \sigma_{\mathrm{RM}} \rangle_{d=0\mathrm{kpc}} = 10.1 \pm 0.2$ to $\langle \sigma_{\mathrm{RM}} \rangle_{d=66\mathrm{kpc}} = 13.9 \pm 0.8$ rad m^{-2}; bottom panel of Figure 7). Hints of these radial trends are also seen in the entire relic (Figure 9; see Appendix C for a view on the beam-sized boxes where we performed the *QU*-fit). In this case, the radial information is obtained by looking at the spectral index, $\alpha_{3.0\mathrm{GHz}}^{150\mathrm{MHz}}$, since steeper values are located farther in the downstream region where synchrotron and inverse Compton energy losses increase (e.g., Di Gennaro et al. 2018). We calculated $\alpha_{3.0\mathrm{GHz}}^{150\mathrm{MHz}}$ using the LOFAR (150 MHz), GMRT (610 MHz), and VLA (1.5 and 3.0 GHz) maps described in Hoang et al. (2017), van Weeren et al. (2010), and Di Gennaro et al. (2018), respectively. We found Pearson and Spearman rank coefficients of $r_p = -0.28$ and $r_s = -0.28$ for the p_0–$\alpha_{3.0\mathrm{GHz}}^{150\mathrm{MHz}}$ distribution and $r_p = 0.16$ and $r_s = 0.24$ for the σ_{RM}–$\alpha_{3.0\mathrm{GHz}}^{150\mathrm{MHz}}$ distribution. These measurements show, for the first time, that the northern relic in CIZAJ2242 suffers from both wavelength- and radial-dependent depolarization.

Finally, no clear downstream variations are seen for the intrinsic polarization angle corrected for the shock normal in the plane of the sky[17] ($\chi_{0,\ \mathrm{corr}} = \chi_0 - n$, second panel of Figure 7) and for the RM (third panel of Figure 7; see also Section 6.5).

[17] Uncertainties on $\chi_{0,\ \mathrm{corr}}$ are determined, including the uncertainties on χ_0 (∼0.01 rad, from the fitting procedure using MCMC) and on n within the beam region (∼0.02 rad at 7″ resolution).

6.2. On the Downstream Depolarization

In the following sections, we discuss two possible explanations for the observed radial profile of the polarization fraction. In particular, we investigate the role of wavelength-dependent depolarization and Faraday rotation (Section 6.2.1) and include a three-dimensional modeling of the relic (Section 6.2.2).

6.2.1. Wavelength-dependent Depolarization and Faraday Rotation Effects

A naive explanation for the downstream depolarization is the effect of a complex magneto-ionic layer that might differently rotate the polarization vectors in different parts of the relic. According to this scenario, the bottom panel of Figure 7 and the right panel of Figure 9 both suggest a mild increasing contribution of the external wavelength-dependent depolarization in the downstream region.

We investigated the relation between the best-fit intrinsic polarization fraction and the measured RM and external wavelength-dependent depolarization (left column of Figure 10). In both cases, we do not see particular trends, nor underlying fluctuations from the analysis of the running median. Both the Pearson and Spearman rank coefficients confirm the visual inspection, with $r_p = -0.06$ and $r_s = -0.09$ for the p_0–RM distribution and $r_p = -0.06$ and $r_s = -0.01$ for the p_0–σ_{RM} one (see Table 4). We therefore conclude that our best-fit intrinsic polarization fraction is independent of external factors, such as the Faraday rotation and the wavelength-dependent depolarization. On the other hand, an anticorrelation in the $p_{1.5\ \mathrm{GHz}}$–σ_{RM} distribution is observed ($r_p = -0.73$ and $r_s = -0.82$). No correlation has been found for the $p_{1.5\mathrm{GHz}}$–RM one ($r_p = -0.07$ and $r_s = -0.04$). These suggest that only the wavelength-dependent depolarization affects the polarization fraction at lower frequencies.

6.2.2. Relic Three-dimensional Shape

For a power-law electron energy distribution with slope $\delta = 1 - 2\alpha$, i.e., $dN(E)/dE \propto E^{-\delta}$, in a region with homogeneous magnetic field the intrinsic polarization amounts to (Rybicki & Lightman 1986)

$$p_0 = \frac{3\delta + 3}{3\delta + 7}. \tag{11}$$

Therefore, if the slope of the electron distribution varies across the relic, the intrinsic polarization will also vary. According to the standard scenario for relic formation, electrons are (re) accelerated at the shock front, with a power-law energy distribution, and cool subsequently owing to synchrotron and inverse Compton energy losses. Locally, the resulting electron spectrum may show a break, even if the sum of all these spectra is a power law again (see Di Gennaro et al. 2018, for a detailed spectral analysis of the relic). The locally curved spectra thus show a different intrinsic degree of polarization than the overall relic. From Equation (11), the downstream region with the aged electron population would have a higher intrinsic polarization fraction (orange line in Figure 11).

Although the decreasing radial profile of the best-fit polarization degree seems to be in contrast with the above description, the complex shape of the shock front and the

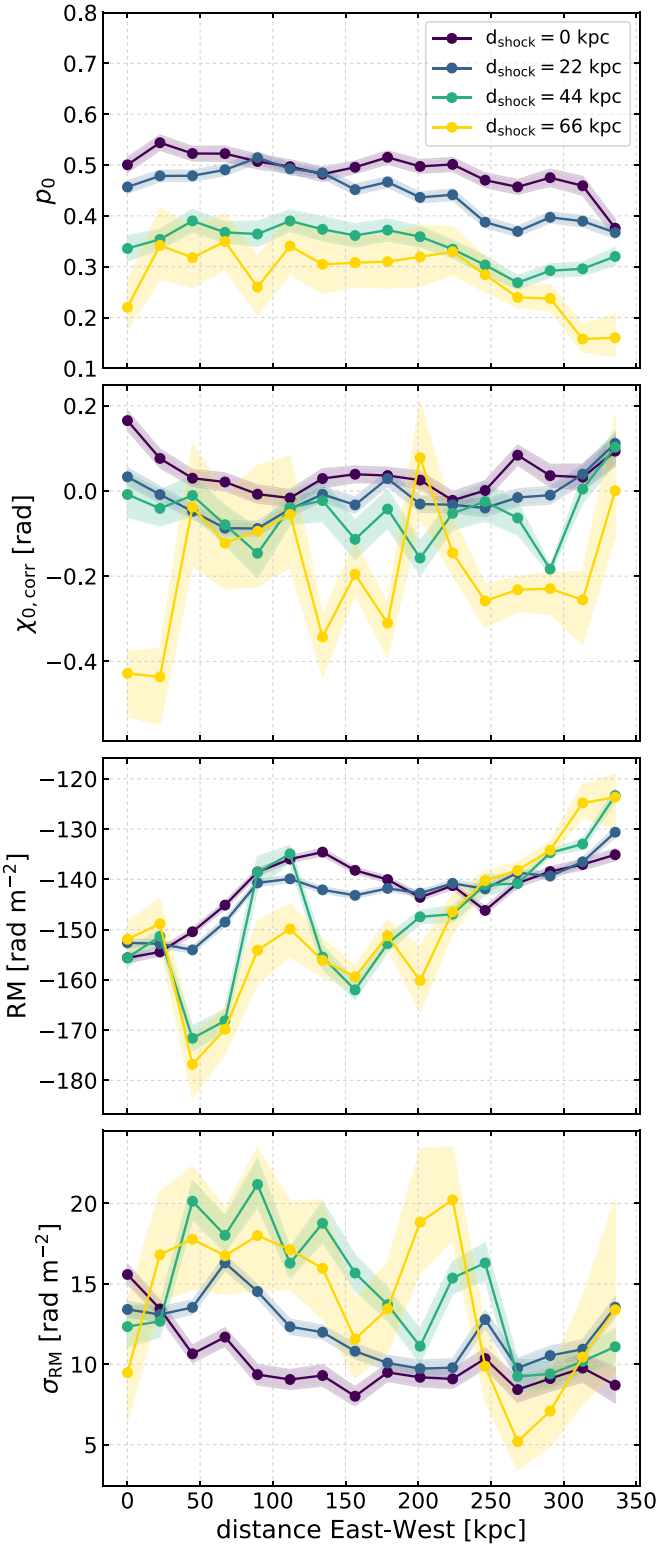

Figure 7. From top to bottom: east–west profiles on the RN3 filament for the best-fit intrinsic polarization fraction (p_0), intrinsic polarization angle corrected for the shock normal ($\chi_{0,\,corr}$), and RM and depolarization (σ_{RM}) using the external Faraday rotation dispersion model (Equation (7)). Different colors represent different distances from the shock (d_{shock}; see legend), with the shock being located at the outermost edge of the relic, and the corresponding shaded areas show the uncertainties on the measurements.

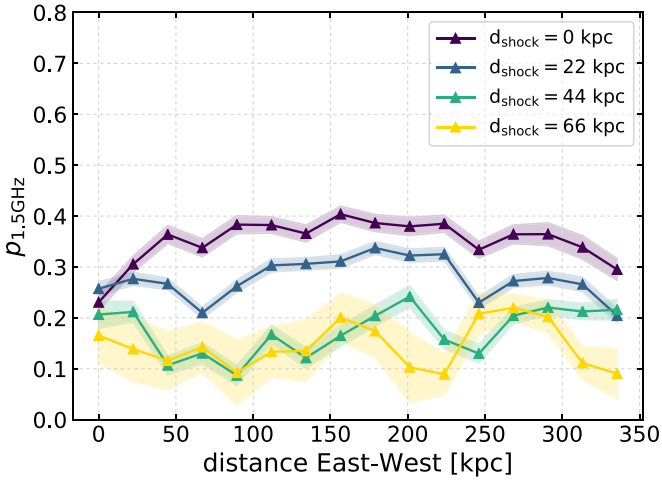

Figure 8. Same as the top panel of Figure 7, but for the polarization fraction at 1.5 GHz.

downstream region may impact the polarization, for instance, by inhomogeneous intrinsic polarization fractions and by large differences in the path through the magnetized ICM from the emission to the observer. In this context, to reproduce a correct projected intrinsic polarization profile, it is necessary to take into account a realistic shape of the shock front, which has to include the contribution of its inclination with respect to the line of sight (M. Hoeft et al., in preparation).

Following Di Gennaro et al. (2018), we created a toy model assuming that the shock front is a spherically symmetric cap in the plane determined by the line of sight and the cluster center, with a curvature radius of 1.5 Mpc and opening angle of $2\psi = 36^\circ$ (see also Figure 10 in Kierdorf et al. 2017). The alignment of electric field vectors with the shock normal (bottom panel of Figure 4) implies that the magnetic field is dominantly tangled on scales smaller than the resolution of the observations (i.e., $2\farcs7$). If the polarization angle reflects the structure of the magnetic field, we can assume a shock compression scenario to explain the polarization properties of the relic (Enßlin et al. 1998). In this scenario, an upstream isotropically tangled magnetic field is compressed by the shock front, resulting in a downstream anisotropically tangled field, causing polarized synchrotron emission. In the specific case of RN, we adopt a shock Mach number of 3.7, which corresponds to an intrinsic polarization fraction of 58%, when the shock is observed perfectly edge-on. This value matches the maximum p_0 we estimated in the relic (see panel (c) of Figure 5). The emission of different parts of the shock front is summed up, taking into account the angle between the shock normal and the line of sight, $90^\circ - \psi$. The more this angle deviates from 90°, the lower the intrinsic polarization becomes. Since those parts of the shock that deviate more from 90° are shifted farther downstream with respect to the outermost edge of the relic, the intrinsic polarization fraction decreases toward the downstream. For our model parameters, these two effects, namely, the downstream increase in polarization due to the aging of the electron population and the decrease due to the shift of those parts of the shock that are not seen perfectly edge-on, cancel out, resulting in an almost constant theoretical p_0 profile. This, however, still deviates from our observations (see blue line and black squares in Figure 11).

It is worth noting that we have used here a very simplified geometrical model that, for instance, does not explain the east–west p_0 variation we observed in the relic. Moreover, it does not include the effect of emitting regions at different Faraday depths in the relic downstream. According to the spherical model described above, at a distance of 60 kpc of the outer

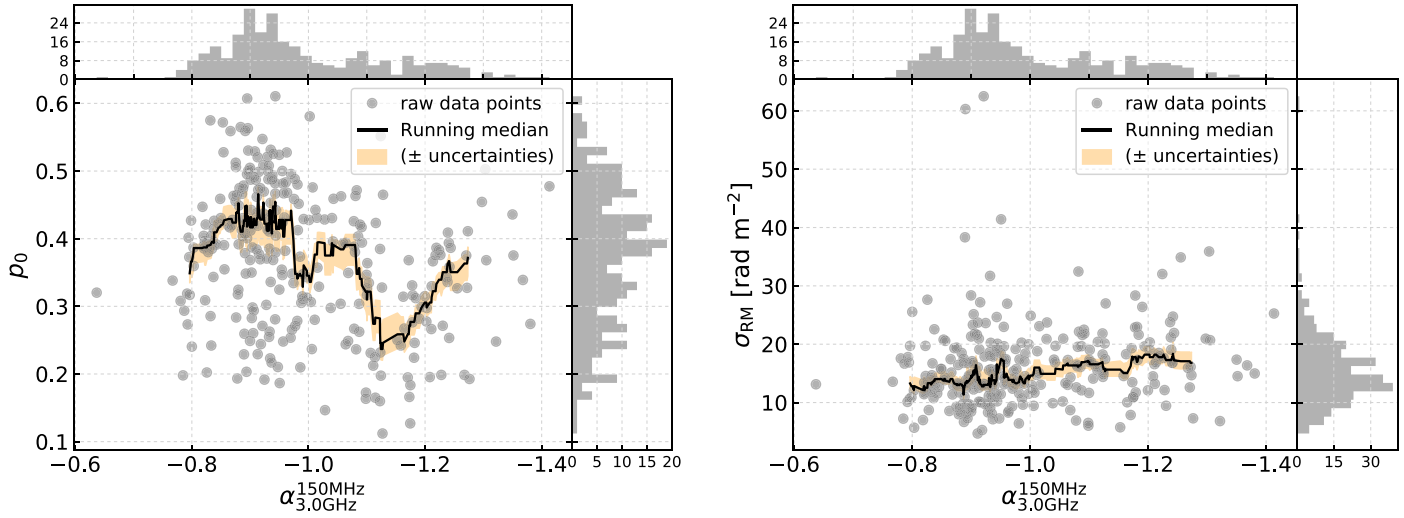

Figure 9. Distributions of the intrinsic polarization fraction and external wavelength-dependent depolarization as a function of the spectral index (gray circles in the left and right panels, respectively). The gray histograms show the projected distribution of the *y*- and *x*-axis quantities along each axis. The black solid line shows the running median of p_0 and $\sigma_{\rm RM}$ calculated using 20 windows in the $\alpha^{150\rm MHz}_{3.0\ \rm GHz}$ space, while the yellow area represents the corresponding uncertainties.

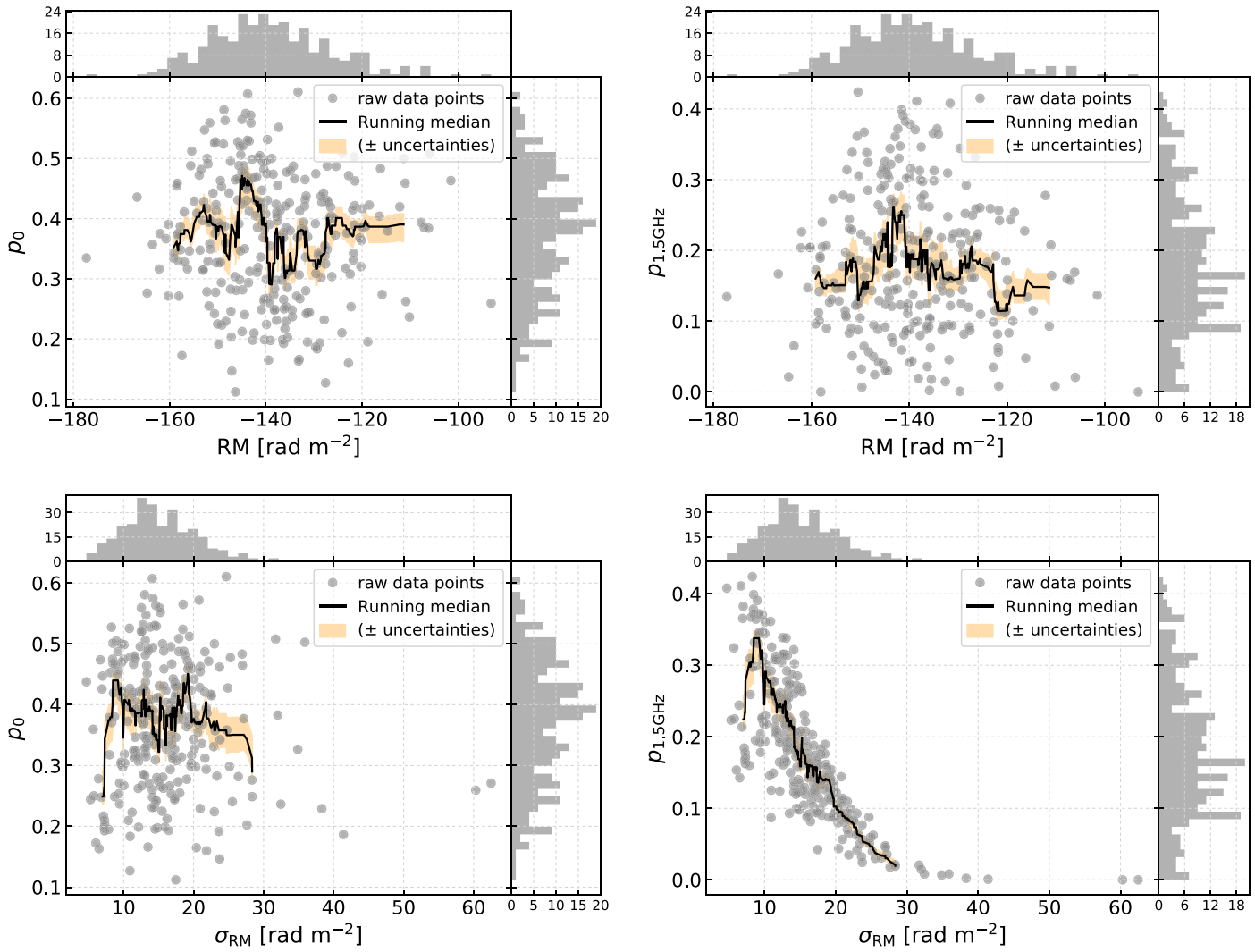

Figure 10. Distributions of the intrinsic and 1.5 GHz polarization fractions (left and right column, respectively) as a function of the absolute relative RM and external wavelength-dependent depolarization (gray circles in the top and bottom panels, respectively). The gray histograms show the projected distribution of the *y*- and *x*-axis quantities along each axis. For both columns, the solid black line represents the running median of the *y*-axis variable (i.e., p_0 and $p_{1.5\ \rm GHz}$) calculated using 20 windows in the space of the *x*-axis variable (i.e., RM and $\sigma_{\rm RM}$). The yellow shaded area represents the uncertainty on the running median.

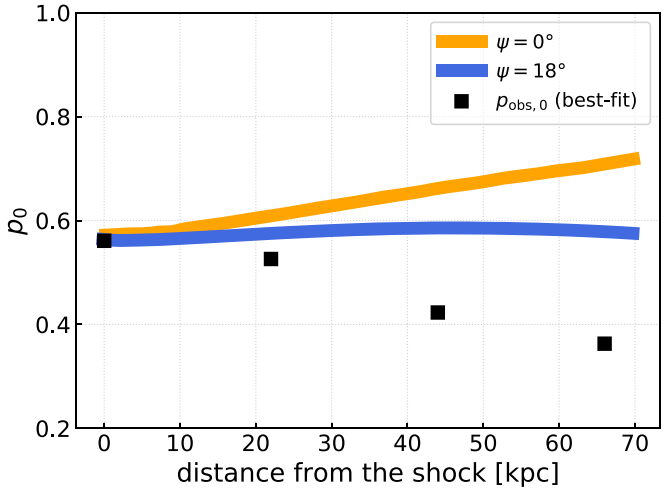

Figure 11. Theoretical profiles of the intrinsic polarization fraction in the post-shock region assuming a shock wave perfectly aligned with the plane of the sky (i.e., $\psi = 0°$; orange line) and assuming an opening angle for the relic of $\psi = 18°$ (Di Gennaro et al. 2018; blue line). Black squares represent the best-fit intrinsic polarization fraction values obtained from a smaller sector of RN3 (i.e., where we could assume constant polarization parameters in the east–west direction).

Table 4
Pearson (r_p) and Spearman (r_s) Rank Correlation Coefficients of the Running Median in Figures 9 and 10

Parameters	r_p	r_s
p_0–RM	−0.06	−0.09
p_0–σ_{RM}	−0.06	−0.01
$p_{1.5GHz}$–RM	−0.07	−0.04
$p_{1.5GHz}$–σ_{RM}	−0.73	−0.82
p_0–$\alpha_{3.0GHz}^{150MHz}$	−0.28	−0.28
σ_{RM}–$\alpha_{3.0GHz}^{150MHz}$	0.16	0.24

edge, the emission from the "back side" of the cluster travels about 800 kpc through the magnetized ICM, which causes additional downstream depolarization. Interestingly, no evidence of multiple-RM components in the downstream region is observed in our data (see Appendix A). This suggests either that the relic cannot be described simply by a smooth spherical cap (e.g., overlapping filamentary structures) or that we might be actually observing only the front/back side of the radio relic. On the other hand, the geometrical projections involve a number of adjustable parameters (see, e.g., Kang et al. 2012). Hence, a detailed modeling, which should include the shock shape, its downstream spectral and polarized characteristics, and its physical properties (such as the Mach number distribution; e.g., Ha et al. 2018; Botteon et al. 2020), is complicated and needs to be further examined.

6.3. Turbulent Magnetic Field in the Post-shock Region

In the presence of both ordered and random magnetic field, Equation (11) can be written as (Sokoloff et al. 1998; Govoni & Feretti 2004)

$$p_0 = \frac{3\delta + 3}{3\delta + 7} \frac{1}{1 + \left(\frac{B_{rand}}{B_{ord}}\right)^2}, \quad (12)$$

where B_{ord} represents the magnetic field component that is aligned with the shock surface and B_{rand} represents the isotropic magnetic field component. Thus, the ratio B_{rand}/B_{ord} describes the order of isotropy of the magnetic field distribution.

In the northern relic of CIZAJ2242, the polarization angle seems to follow well the shock normal (see bottom panel of Figure 4), and no change is observed in the downstream region (second panel of Figure 7). This suggests that the component of the magnetic field parallel to the polarization angle is approximately constant in the downstream region. However, our measurements are limited by the observing resolution, which can hide the presence of tangled magnetic field on smaller scales and lead to a decreasing polarization fraction. If this is the case, from Equation (12) we can relate the radial decrease of p_0 to the decrease of the degree of anisotropy in the downstream region (i.e., the ratio B_{rand}/B_{ord} increases). Given the averaged values found in the RN3 filament, i.e., $\langle p_0 \rangle_{d=0kpc} \sim 0.49$ and $\langle p_0 \rangle_{d=66kpc} \sim 0.28$, and assuming $\delta = 3$ (i.e., $\alpha = -1$), we find that the ratio B_{rand}/B_{ord} should increase by about 40% in the downstream region. Shock propagation in the ICM generates vorticity that boosts turbulence and amplifies the magnetic field (e.g., Ryu et al. 2008). Behind the shock, turbulence behaves more or less as a "decaying" turbulence (see, e.g., Porter et al. 2015; Donnert et al. 2018), which might lead to the decreasing degree of anisotropy. Further studies are needed, however, on this point.

The turbulent magnetic field B_{turb} is related to the wavelength-dependent depolarization, according to (Sokoloff et al. 1998; Kierdorf et al. 2017)

$$\sigma_{RM} = 0.81 \sqrt{\frac{1}{3}} \langle n_e \rangle B_{turb} \sqrt{\frac{L\Lambda}{f}}, \quad (13)$$

where $\langle n_e \rangle$ is the average electron density in cm^{-3}, f is the volume filling factor of the Faraday-rotating gas, L is the path length through the thermal gas, and Λ is the turbulence scale, with the last two in units of pc. In the cluster area, only source O is a background polarized radio galaxy (see Figure 12). From our QU-fit, we found that the amount of the external depolarization for this source is very similar to that in RN, i.e., $\sigma_{RM} \sim 22$ rad m^{-2} (see panel (f) of Figure 5 and bottom left panel of Figure 6). Given the proximity of source O and RN and assuming that there is no contribution to the depolarization from source O itself and from the Galactic plane, we can use this σ_{RM} in Equation (13) to obtain an approximate estimation of the tangled magnetic field in the northern relic, being $B_{turb} \sim 5.6\,\mu$G. Here we used $\langle n_e \rangle = 10^{-4}$ cm^{-3} (Ogrean et al. 2014), $L = 350$ kpc[18], $f = 0.5$ (Govoni & Feretti 2004; Murgia et al. 2004), and $\Lambda = 8$ kpc[19], i.e., the linear scale of our best-resolution observation (i.e., 2.″7). Note that the estimated B_{turb} is consistent with the upper value of the total magnetic field strength quoted by van Weeren et al. (2010), leading to a ratio of magnetic and thermal pressures $P_{mag}/P_{th} \sim 0.11$ (Akamatsu et al. 2015).

6.4. Effect of the Limited Frequency Band Coverage

The basic assumption of the QU-fitting approach is that, given observations in a wide band $\Delta\lambda^2 = \lambda^2_{max} - \lambda^2_{min}$ and

[18] The path length of the magnetized plasma crossed by the polarized emission is $L \approx 2\sqrt{2 d_s\, r_s}$, where $d_s = 10$ kpc and $r_s = 1.5$ Mpc are the intrinsic width of the shock and its distance from the cluster center, respectively (see Kierdorf et al. 2017).

[19] This is about one order of magnitude smaller than what is commonly used for galaxy clusters (i.e., 100 kpc; see Iapichino & Brüggen 2012).

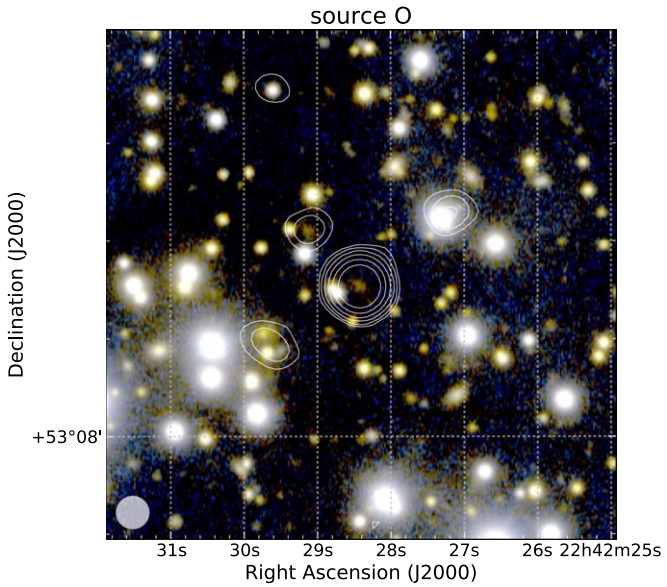

Figure 12. Subaru *g-gi-i* optical image of source O (Dawson et al. 2015; Jee et al. 2015). The 1–4 GHz total intensity radio contours at 2.″5 resolution are overlaid at levels of $3\sigma_{\rm rms} = \sqrt{(1,\ 4,\ 16,...)}$, with $\sigma_{\rm rms} = 5.6\ \mu$Jy beam^{-1} the map noise (Di Gennaro et al. 2018).

assuming a theoretical model, one can extrapolate the intrinsic polarization parameters, p_0 and χ_0, at the ideal wavelength $\lambda \to 0$, where no wavelength-dependent effects (e.g., depolarization or Faraday rotation) occur. The wider $\Delta\lambda^2$ and the lower $\lambda^2_{\rm min}$, the better one can validate the theoretical model. However, due to the lack of high-resolution information at higher frequencies, we cannot exclude the possibility of the existence of a more complex model to describe the polarized emission in RN. For example, Ozawa et al. (2015) found a step-like fractional polarization profile in the radio relic in Abell 2256, with the fractional polarization increase occurring above 3.0 GHz. However, it is important to note that the presence of more complex models would result in a strong deviation from the Burn model in the downstream region, where a larger amount of magnetized plasma (i.e., the ICM) is crossed. Despite the low S/N, however, we see that the Burn approximation still holds in this region. Finally, $\Delta\lambda^2$ also sets the amount of wavelength-dependent depolarization detectable. Given our observing band, it would be rather difficult to determine $p(\lambda^2)$ if $\sigma_{\rm RM} \geqslant 100$ rad m^{-2}.

Interestingly, if we extract the profiles of the polarization parameters using an internal Faraday rotation dispersion model (i.e., Equation (8)), we find consistent p_0, χ_0, and RM profiles with those we found using the external depolarization model and a larger amount of internal depolarization $\varsigma_{\rm RM}$, in agreement with the mathematical differences of the two formulae. This means that, with the current data in hand, we cannot distinguish between an external and an internal depolarization model for the northern relic in CIZAJ2242. Lower-wavelength wide-band observations (i.e., C and X bands, 4–8 GHz and 8–12 GHz, respectively) might then help to infer the nature of the polarized emission of the northern relic in CIZAJ2242.

6.5. Investigation for Intrinsic RM Fluctuations

We found very weak/no correlations between RM and the spectral index and between RM and the external wavelength-dependent depolarization (Figures 13 and 14, respectively, and Table 5). The absence of correlation in the latter case is expected in the case of external beam depolarization (Govoni & Feretti 2004).

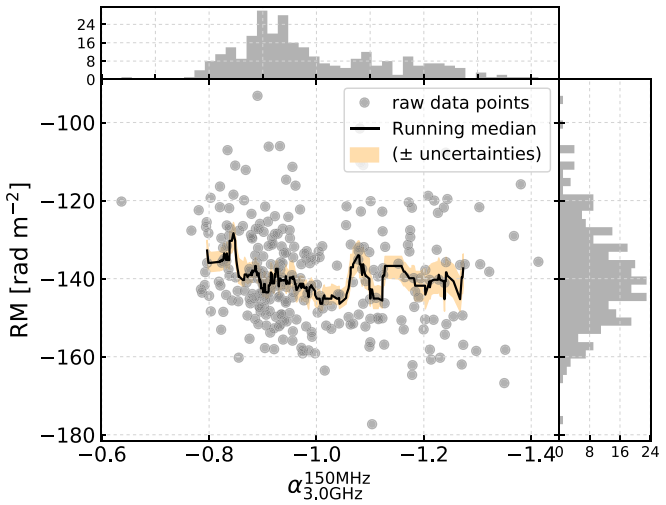

Figure 13. Distributions of the absolute relative RM as a function of the spectral index (gray circles). The gray histograms show the projected distribution of the *y*- and *x*-axis quantities along each axis. The black solid line shows the running median of RM in the $\alpha^{150\rm MHz}_{3.0\rm GHz}$ space using 20 windows. The yellow area represents the uncertainties on the running median.

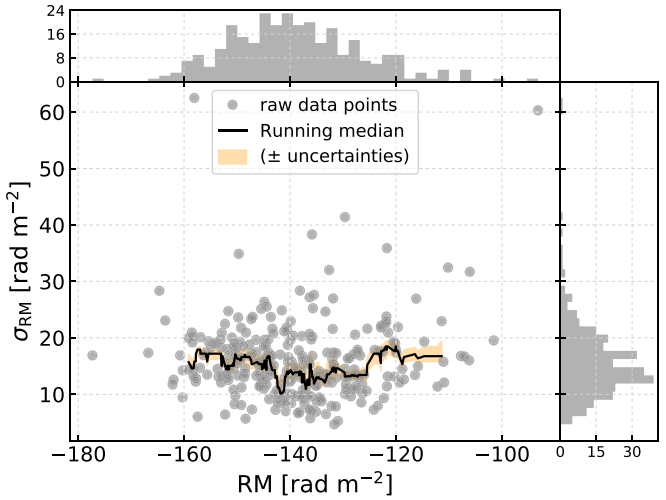

Figure 14. Distribution of the external wavelength-dependent depolarization as a function of the absolute relative RM (gray circles). The gray histograms show the projected distribution of the *y*- and *x*-axis quantities along each axis. The black solid line shows the running median of $\sigma_{\rm RM}$ in the RM space calculated using 20 windows. The yellow area represents the uncertainties on the running median.

In Section 4, we show evidence for strong RM variation of the Galactic foreground, over angular scales of $\mathbf{3'-5'}$, by investigating the RM values in radio galaxies outside the cluster. Along the northern relic, a variation of 30 rad m^{-2} around the median value of 140.8 rad m^{-2} is also found on much smaller scales (i.e., $\mathbf{15''-30''}$; see Figure 5). At the cluster position ($\boldsymbol{l} = \mathbf{104}°$ and $\boldsymbol{b} = -\mathbf{5}°$), strong variation from the Galactic plane is expected (C. van Eck 2021, private communication), although detailed studies are still missing. If the detected RM variation is entirely due to the Galactic plane,

Table 5
Pearson (r_p) and Spearman (r_s) Rank Correlation Coefficients of the Running Median in Figures 13 and 14

Parameters	r_p	r_s
RM–$\alpha_{3.0\,\mathrm{GHz}}^{150\,\mathrm{MHz}}$	−0.14	−0.17
σ_{RM}–RM	0.08	−0.05

this would show for the first time that Galactic RM variation is also present on relatively small scales.

Alternatively, this variation could be due to the ICM and to the magnetic field close to the relic. As shown in Figures 5 and 6, the strongest RM fluctuations are measured at the connection of two pairs of filaments, i.e., RN1–RN2 and RN3–RN4, where we measure on average $\Delta\mathrm{RM} \sim 30\,\mathrm{rad\,m^{-2}}$ (see panel (e) of Figure 5). If this is entirely due to the ICM, given the relation between RM and $B_{\parallel}$ (Equation (5)), we can constrain the magnetic field variation in the relic, with $\Delta B_{\parallel} \sim 1\,\mu$G, where we have used $n_e = 10^{-4}\,\mathrm{cm^{-3}}$ and $L = 350\,\mathrm{kpc}$. Assuming a global value of 5 μG (van Weeren et al. 2010), we obtain a magnetic field variation of roughly 20%. In the case of weaker global magnetic field, i.e., 1.2 μG (van Weeren et al. 2010), variations increase up to 80%.

7. Conclusions

In this work, we have presented a polarimetric study of the merging galaxy cluster CIZA J2242.8+5301 ($z = 0.1921$) in the 1–4 GHz frequency range with the VLA. We used the *QU*-fitting approach to obtain information on the polarization parameters, i.e., intrinsic polarization fraction (p_0), intrinsic polarization angle (χ_0), RM, and depolarization (σ_{RM}), for the full cluster at 2.″7, 4.″5, 7″, and 13″ resolution. This work mainly focused on the most prominent source in CIZA J2242.8+5301, i.e., the northern radio relic (RN). Below, we summarize the main results of our work:

1. CIZA J2242.8+5301 is bright in polarized light, with the emission coming from several sources, both diffuse and associated with radio galaxies. In particular, at the highest resolution available (i.e., 2.″7) the northern relic mimics the filamentary structure seen in total intensity emission (Di Gennaro et al. 2018).
2. In agreement with previous studies (van Weeren et al. 2010; Kierdorf et al. 2017), we found a high degree of intrinsic polarization in RN, with the eastern side having a higher value than the western one (i.e., $p_{0,\ \mathrm{east}} \sim 0.55$ and $p_{0,\ \mathrm{west}} \sim 0.35$, with p_0 the best-fit values from the *QU*-fit).
3. The polarization vectors strongly align with the shock surface also in high-resolution observations (i.e., 2.″7), implying that the magnetic field is dominantly tangled on scales smaller than ∼8 kpc.
4. For the first time we were able to investigate the polarization parameters in the relic post-shock region on tens-of-kiloparsec scales. We found that both the best-fit intrinsic and 1.5 GHz polarization fractions (i.e., p_0 and $p_{1.5\mathrm{GHz}}$) decrease toward the cluster center. While for the latter a strong contribution of the external wavelength-dependent depolarization is present, the downstream depolarization profile for p_0 does not correlate with RM and σ_{RM}.
5. We speculate that complex geometrical projections and/or relic shape could possibly explain the p_0 downstream depolarization, although detailed modelings should be further worked. We also note that the decrease of the degree of magnetic field anisotropies (i.e., $B_{\mathrm{ord}}/B_{\mathrm{rand}}$) by about 40% might explain the depolarization.
6. We detect only one polarized background radio galaxy, i.e., source O. Its σ_{RM} is similar to the average value in the northern relic and allows us to set an approximate value on the turbulent cluster magnetic field of about 5.6 μG.
7. Different RMs are observed in the northern and southern relics ($\mathrm{RM_{RN}} \sim -140\,\mathrm{rad\,m^{-2}}$ and $\mathrm{RM_{RS}} \sim -80\,\mathrm{rad\,m^{-2}}$, respectively). This could be due to either variation of the foreground Galactic Faraday rotation or a different contribution of $n_e B_{\parallel}$ in the ICM along the line of sight.
8. RM fluctuations of about $30\,\mathrm{rad\,m^{-2}}$ on physical scales of about $\mathbf{3'-5'}$ are observed at the location of the northern relic. With the current data in hand we cannot determine whether this is due to the Galactic plane or to magnetic field local to the relic. In the former case, this will be the first evidence of small-scale Galactic RM fluctuations. In the latter case, we estimate a magnetic field variation of about 1 μG.

Recently, the polarization properties of radio relics were investigated by Wittor et al. (2019) and Roh et al. (2019) using numerical simulations. Although they were able to reproduce some properties of observed relics, such as the global observed degree of polarization, they found that it is difficult to explain the high-degree polarization (up to ∼60%) and the uniformity of the intrinsic polarization angle of the Sausage relic. Incorporating realistic modelings, as well as matching the spatial resolution for simulations and observations, would be crucial steps for the understanding of the observed polarization properties of relics and the connection to the underlying magnetic field.

G.D.G. and R.J.v.W. acknowledge support from the ERC Starting Grant ClusterWeb 804208. H.J.A.R. acknowledges support from the ERC Advanced Investigator program New-Clusters 321271. R.J.v.W. acknowledges support of the VIDI research program with project No. 639.042.729, which is financed by the Netherlands Organisation for Scientific Research (NWO). Partial support for L.R. comes from U.S. National Science Foundation grant AST 17-14205 to the University of Minnesota. D.R. acknowledges support from the National Research Foundation of Korea through grants 2016R1A5A1013277 and 2020R1A2C2102800. A.S. acknowledges support through a Clay Fellowship administered by the Smithsonian Astrophysical Observatory. W.F., C.J., and R.P.K. acknowledge support from the Smithsonian Institution and the Chandra High Resolution Camera Project through NASA contract NAS8-03060. D.N.H acknowledges support from the ERC through grant ERC-Stg DRANOEL n. 714245. This research made use of APLpy, an open-source plotting package for Python (Robitaille & Bressert 2012).

Appendix A
QU-fit Plots

In Figure 1 we show an example of the *QU*-fitting results on a single pixel with high S/N at the shock location. In

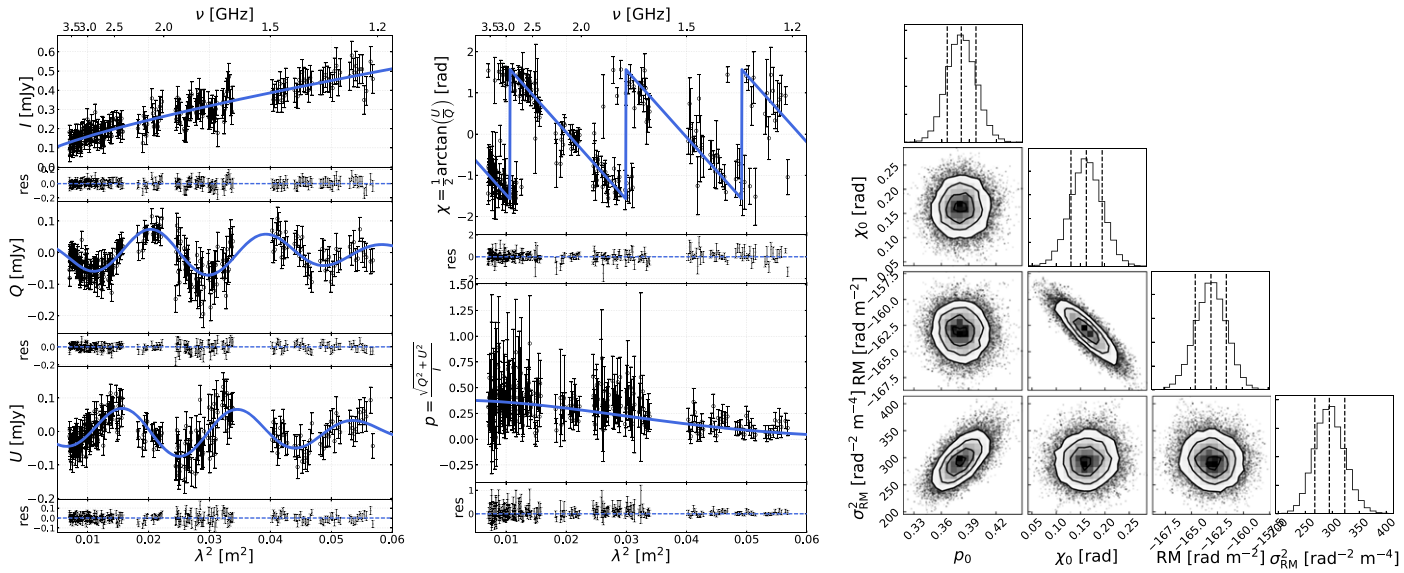

Figure A1. Same as Figure 1, but for a pixel farther in the RN downstream region.

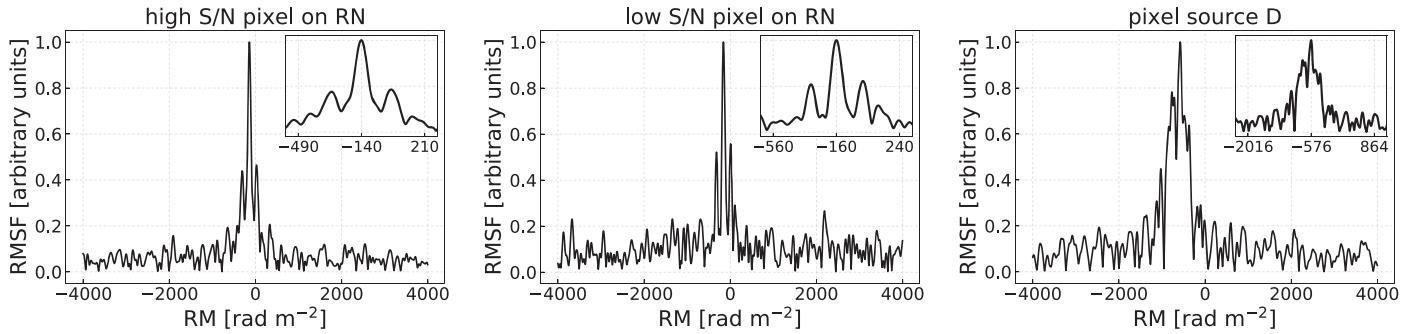

Figure A2. Faraday spectrum on the pixels displayed in Figures 1 (left panel) and A1 (middle panel). In the right panel, the Faraday spectrum of a high-S/N pixel in source D is shown. The inset in the plots shows the zoom-in on the Faraday peak.

Figure A1, we show the same results but applied on a pixel in the relic downstream. Despite the lower S/N, a single-RM component QU-fit still provides a good match to our data. In Figure A2, we show the Faraday spectrum on these two pixels, obtained with `pyrmsynth`. The RM cube ranges from -4000 to $+4000\,\mathrm{rad\,m^{-2}}$, with an FWHM of $60\,\mathrm{rad\,m^{-2}}$. The two symmetric sidelobes we see next to each peak are likely due to interference in the Faraday spectra, as we do not use the `RM-CLEAN` option (see footnote 2 in Brentjens 2011).

Appendix B
Uncertainty Maps on the Polarization Parameters

In this appendix we show the p_0, RM, and σ_{RM} negative and positive uncertainty maps corresponding to Figures 5(d), (e), and (f) (right and left columns of Figure B1) and the $p_{1.5\,\mathrm{GHz}}$ uncertainty maps (Figure B2). We also present the polarization parameter uncertainty (negative and positive) maps of the full cluster at 13″ resolution (Figures B3 and B4). The map of the polarization fraction at 1.5 GHz and its corresponding uncertainty map of the full cluster at 7″ resolution are displayed in Figure B5.

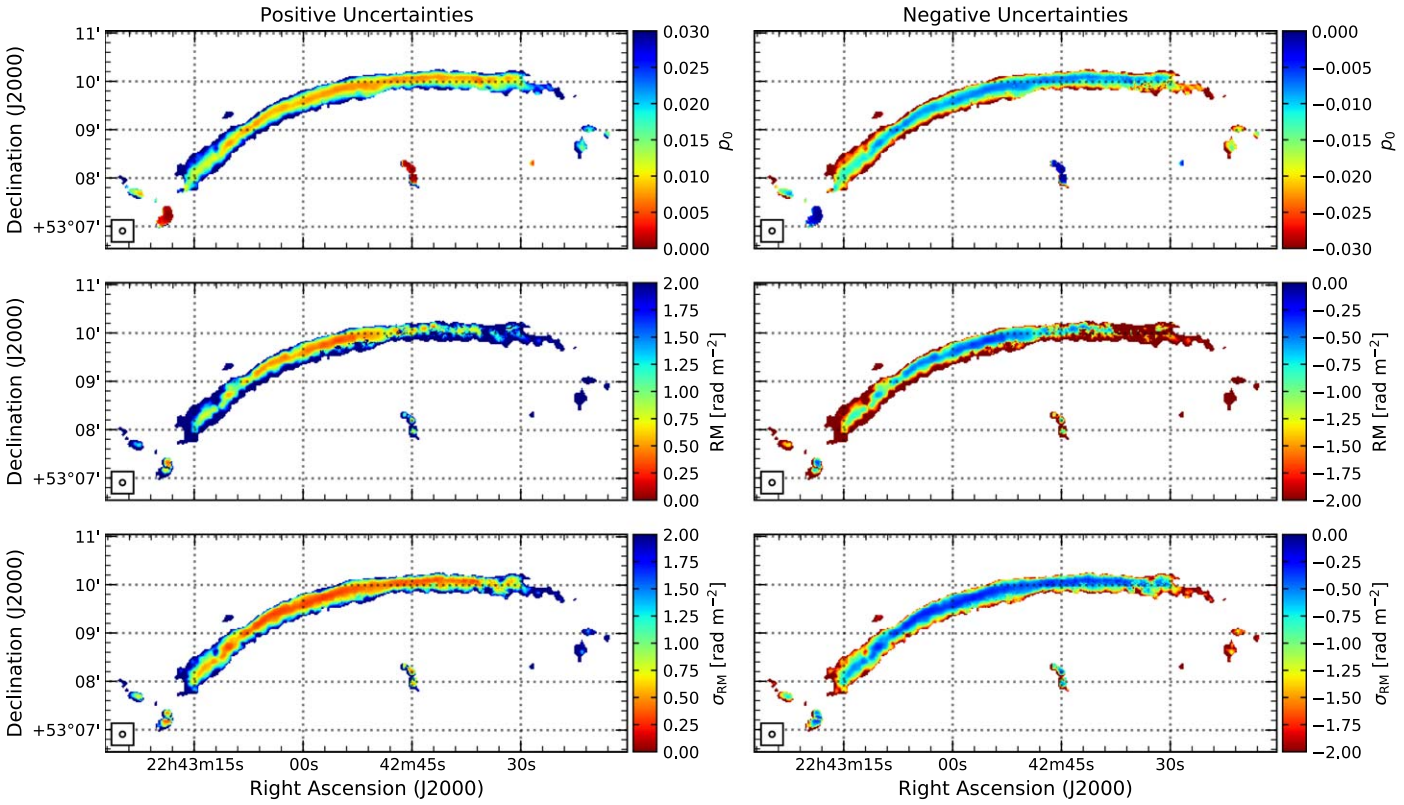

Figure B1. Positive (left column) and negative (right column) uncertainty maps corresponding to panels (c), (e), and (f) of Figure 5.

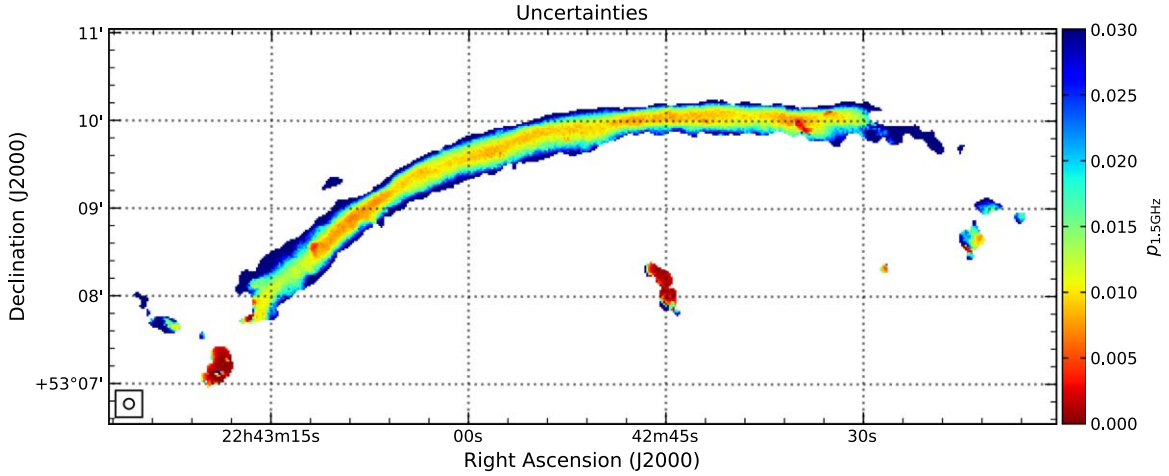

Figure B2. 1.5 GHz polarization fraction uncertainty map (panel (d) of Figure 5).

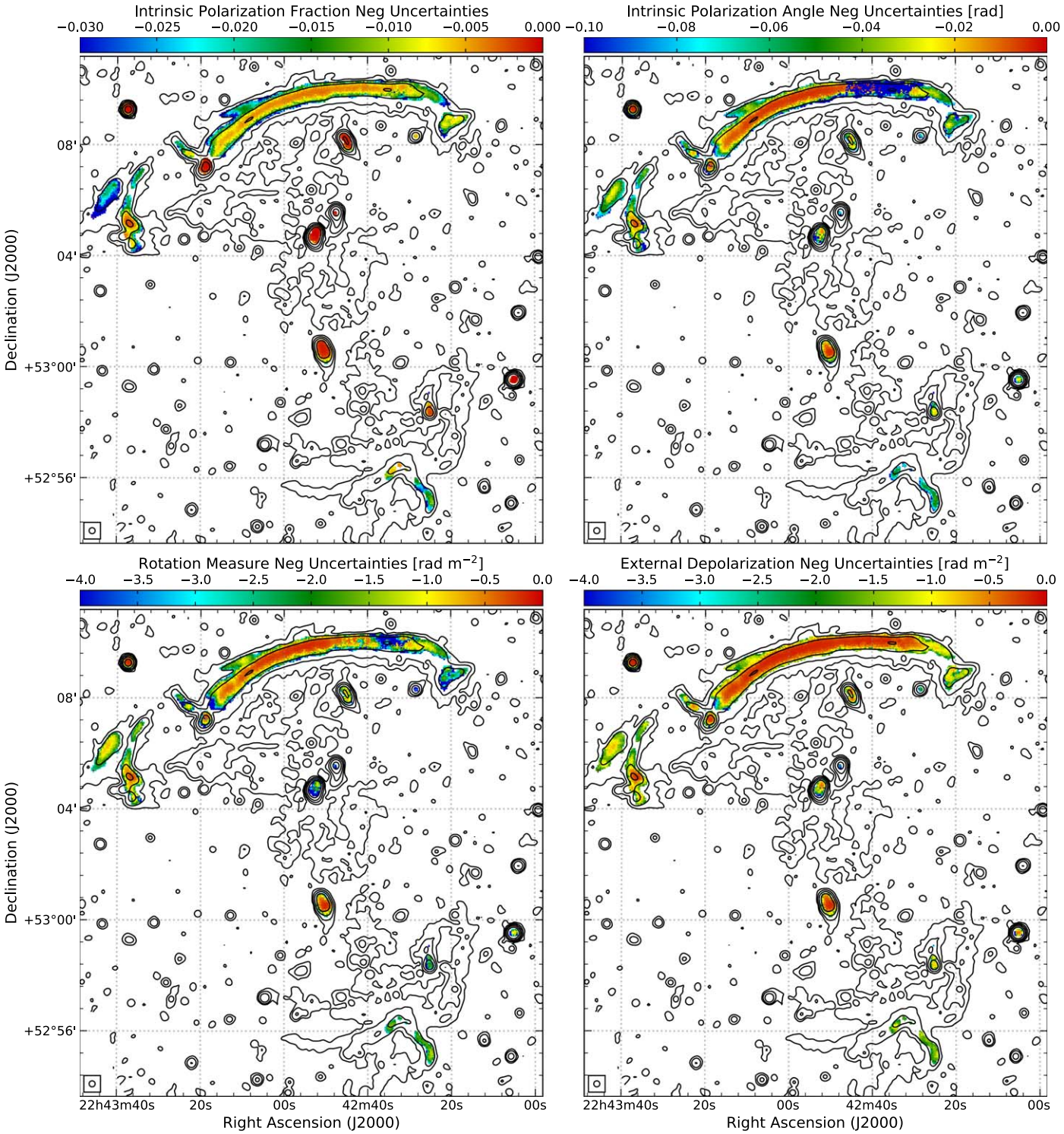

Figure B3. Negative uncertainty maps corresponding to Figure 6.

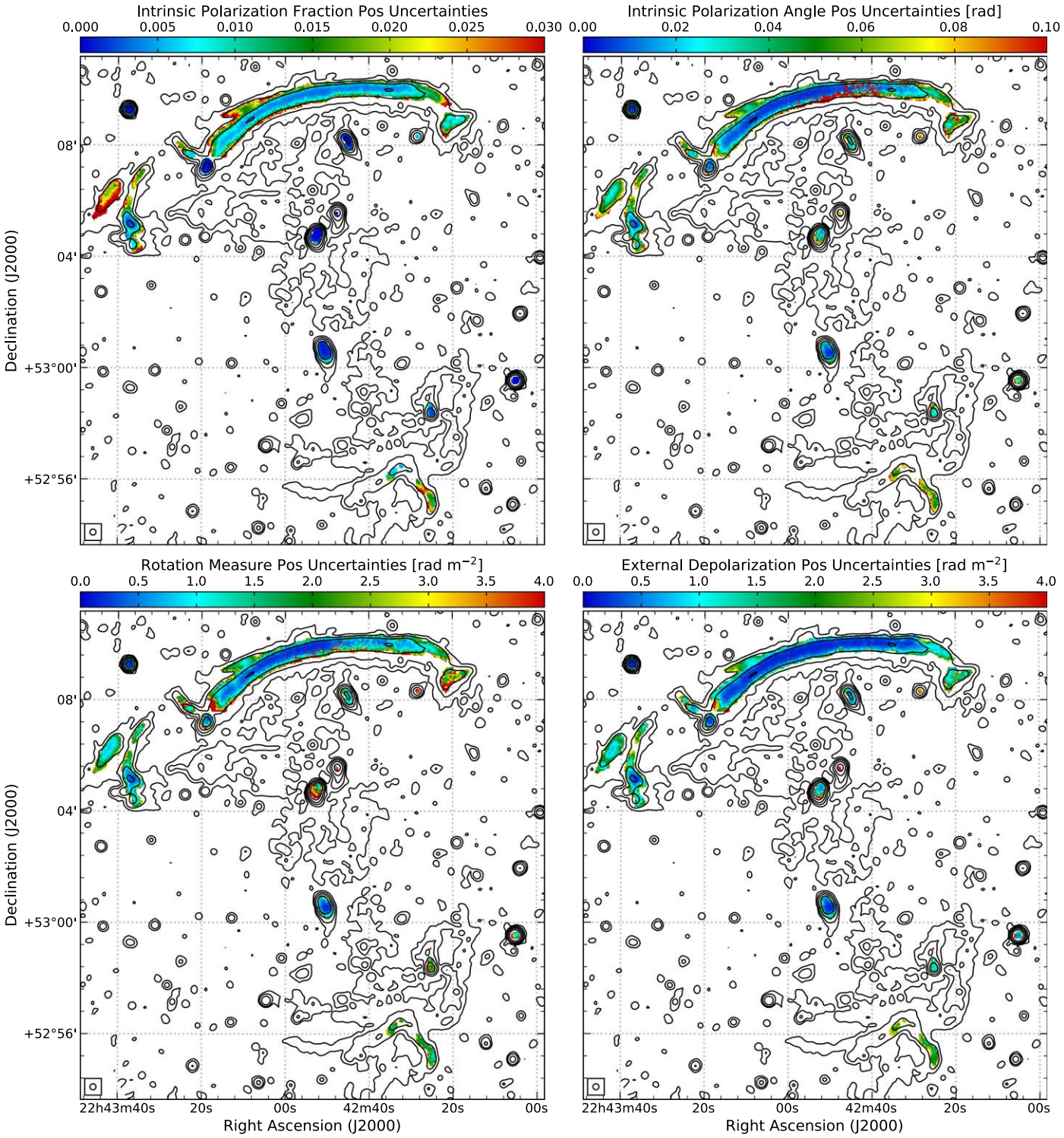

Figure B4. Positive (bottom panel) uncertainty maps corresponding to Figure 6.

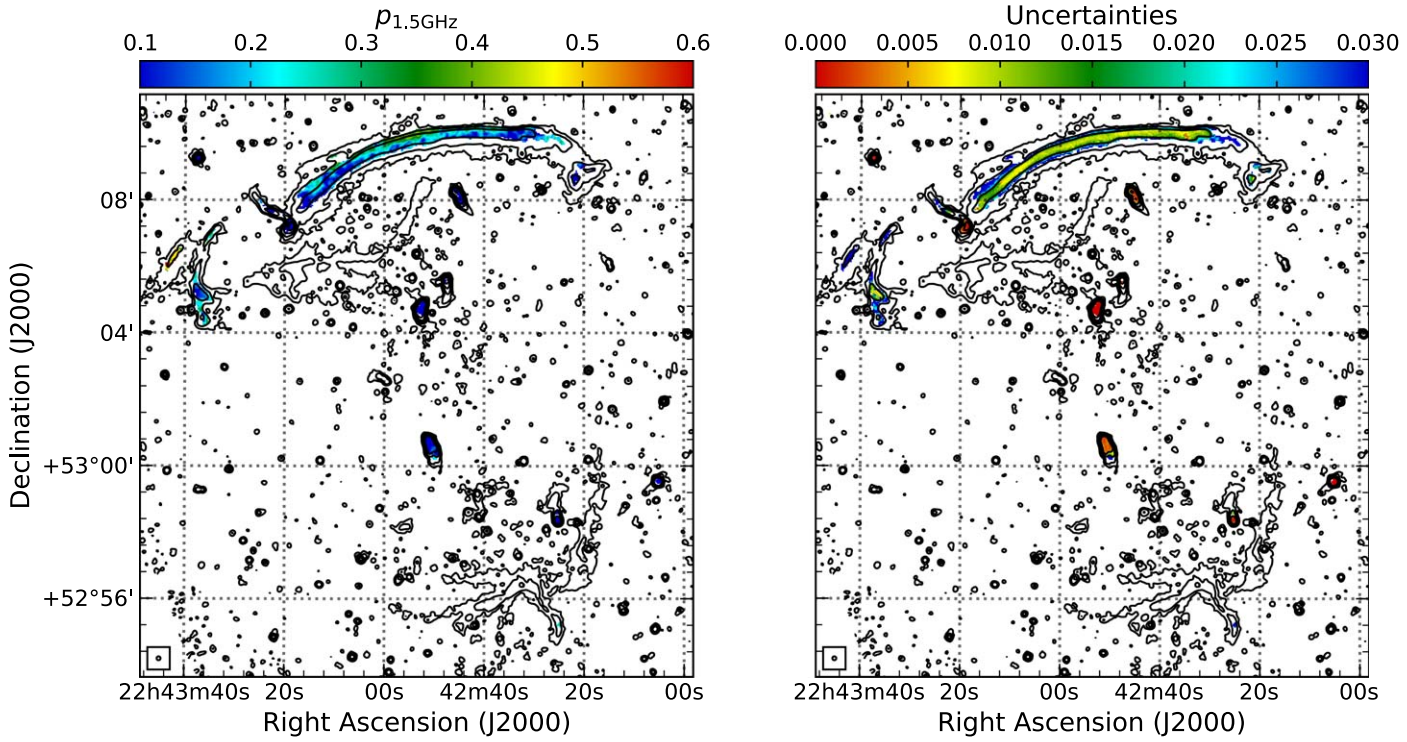

Figure B5. Polarization fraction map at 1.5 GHz (left panel) and corresponding error map (right panel) of CIZAJ2242 at 7″ resolution. Stokes *I* radio contours at the same resolution are drawn in black at the level of $3\sigma_{\rm rms}\sqrt{1, 4, 16, 64,...}$, with $\sigma_{\rm rms} = 4.2$ μJy beam^{-1} (Di Gennaro et al. 2018).

Appendix C
Annuli on RN3 and Grid Used for the Correlation Analysis

Here we display the regions where we performed the *QU*-fit. The boxes shown in Figure C1 generate the profiles in Figures 7 and 8. The boxes shown in Figure C2 generate Figures 9, 10, 13, and 14. Each box has the same size of the restoring beam, i.e., 7″ × 7″ (about 22 × 22 kpc^2 at the cluster redshift). The polarized flux in each box is above a threshold of $3\sigma_{{\rm rms},P}$ (see Section 3).

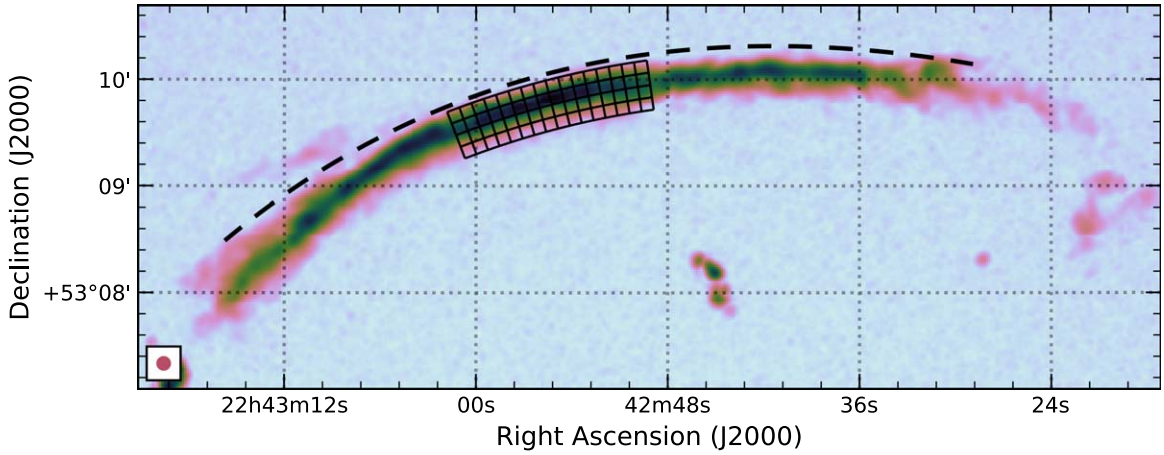

Figure C1. Total averaged polarization image at 7″ resolution of the northern relic, with the boxes used to investigate the presence correlation among the polarization parameters in Figures 7 and 8. The position of the shock (i.e., $d_{\rm shock} = 0$ kpc) is displayed by the black dashed line.

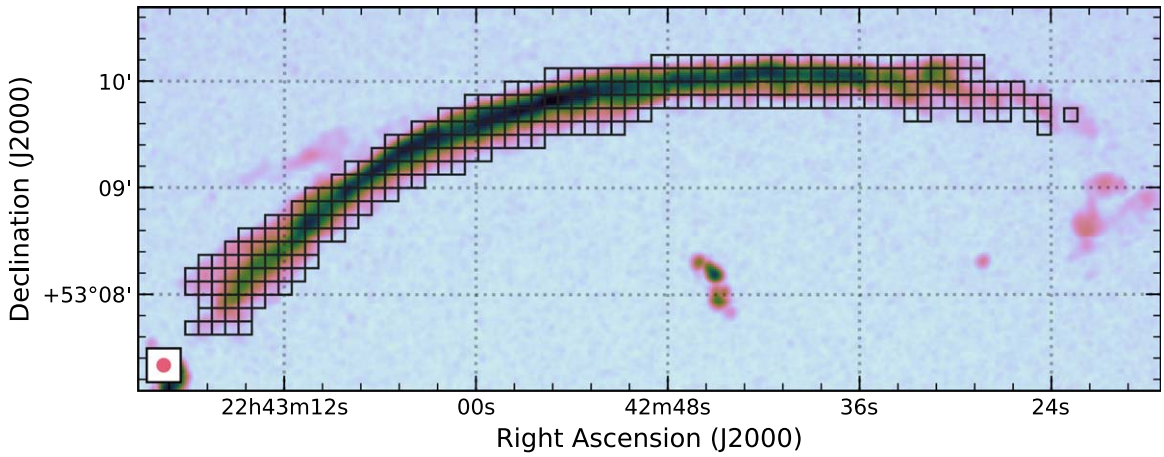

Figure C2. Total averaged polarization image at 7″ resolution of the northern relic, with the boxes used to investigate the presence of correlation among the polarization parameters in Figures 10 and 14.

ORCID iDs

G. Di Gennaro https://orcid.org/0000-0002-8648-8507
R. J. van Weeren https://orcid.org/0000-0002-0587-1660
L. Rudnick https://orcid.org/0000-0001-5636-7213
M. Hoeft https://orcid.org/0000-0001-5571-1369
M. Brüggen https://orcid.org/0000-0002-3369-7735
Dongsu Ryu https://orcid.org/0000-0002-5455-2957
H. J. A. Röttgering https://orcid.org/0000-0001-8887-2257
W. Forman https://orcid.org/0000-0002-9478-1682
A. Stroe https://orcid.org/0000-0001-8322-4162
T. W. Shimwell https://orcid.org/0000-0001-5648-9069
R. P. Kraft https://orcid.org/0000-0002-0765-0511
C. Jones https://orcid.org/0000-0003-2206-4243
D. N. Hoang https://orcid.org/0000-0002-8286-646X

References

Akamatsu, H., van Weeren, R. J., Ogrean, G. A., et al. 2015, A&A, 582, A87
Anderson, C. S., Gaensler, B. M., & Feain, I. J. 2016, ApJ, 825, 59
Basu, K., Vazza, F., Erler, J., & Sommer, M. 2016, A&A, 591, A142
Bicknell, G. V., Cameron, R. A., & Gingold, R. A. 1990, ApJ, 357, 373
Bonafede, A., Feretti, L., Murgia, M., et al. 2010a, A&A, 513, A30
Bonafede, A., Feretti, L., Murgia, M., et al. 2010b, arXiv:1009.1233
Bonafede, A., Vazza, F., Brüggen, M., et al. 2013, MNRAS, 433, 3208
Botteon, A., Brunetti, G., Ryu, D., & Roh, S. 2020, A&A, 634, A64
Brentjens, M. A. 2011, A&A, 526, A9
Brentjens, M. A., & de Bruyn, A. G. 2005, A&A, 441, 1217
Brüggen, M., Ruszkowski, M., Simionescu, A., Hoeft, M., & Dalla Vecchia, C. 2005, ApJL, 631, L21
Brunetti, G., & Jones, T. W. 2014, IJMPD, 23, 1430007
Burn, B. J. 1966, MNRAS, 133, 67
Dawson, W. A., Jee, M. J., Stroe, A., et al. 2015, ApJ, 805, 143
Di Gennaro, G., van Weeren, R. J., Hoeft, M., et al. 2018, ApJ, 865, 24
Dolag, K., Bartelmann, M., & Lesch, H. 1999, A&A, 348, 351
Donnert, J., Vazza, F., Brüggen, M., & ZuHone, J. 2018, SSRv, 214, 122
Donnert, J. M. F., Beck, A. M., Dolag, K., & Röttgering, H. J. A. 2017, MNRAS, 471, 4587
Donnert, J. M. F., Stroe, A., Brunetti, G., Hoang, D., & Roettgering, H. 2016, MNRAS, 462, 2014
Enßlin, T. A., Biermann, P. L., Klein, U., & Kohle, S. 1998, A&A, 332, 395
Farnsworth, D., Rudnick, L., & Brown, S. 2011, AJ, 141, 191
Foreman-Mackey, D., Hogg, D. W., Lang, D., & Goodman, J. 2013, PASP, 125, 306
Frick, P., Sokoloff, D., Stepanov, R., & Beck, R. 2011, MNRAS, 414, 2540
Fujita, Y., Takizawa, M., Yamazaki, R., Akamatsu, H., & Ohno, H. 2015, ApJ, 815, 116
Govoni, F., & Feretti, L. 2004, IJMPD, 13, 1549
Govoni, F., Murgia, M., Feretti, L., et al. 2006, A&A, 460, 425
Ha, J.-H., Ryu, D., & Kang, H. 2018, ApJ, 857, 26
Hoang, D. N., Shimwell, T. W., Stroe, A., et al. 2017, MNRAS, 471, 1107
Iapichino, L., & Brüggen, M. 2012, MNRAS, 423, 2781
Jee, M. J., Stroe, A., Dawson, W., et al. 2015, ApJ, 802, 46
Kang, H., & Ryu, D. 2016, ApJ, 823, 13
Kang, H., Ryu, D., & Jones, T. W. 2012, ApJ, 756, 97
Kang, H., Ryu, D., & Jones, T. W. 2017, ICRC (Busan, Korea), 35, 283
Kierdorf, M., Beck, R., Hoeft, M., et al. 2017, A&A, 600, A18
Kocevski, D. D., Ebeling, H., Mullis, C. R., & Tully, R. B. 2007, ApJ, 662, 224
Lamee, M., Rudnick, L., Farnes, J. S., et al. 2016, ApJ, 829, 5
Loi, F., Murgia, M., Govoni, F., et al. 2017, MNRAS, 472, 3605
Massaro, E., Perri, M., Giommi, P., & Nesci, R. 2004, A&A, 413, 489
Murgia, M., Govoni, F., Feretti, L., et al. 2004, A&A, 424, 429
Offringa, A. R., de Bruyn, A. G., Biehl, M., et al. 2010, MNRAS, 405, 155
Offringa, A. R., McKinley, B., Hurley-Walker, N., et al. 2014, MNRAS, 444, 606
Ogrean, G. A., Brüggen, M., van Weeren, R., et al. 2014, MNRAS, 440, 3416
Oppermann, N., Junklewitz, H., Greiner, M., et al. 2015, A&A, 575, A118
Orrù, E., van Velzen, S., Pizzo, R. F., et al. 2015, A&A, 584, A112
O'Sullivan, S. P., Brown, S., Robishaw, T., et al. 2012, MNRAS, 421, 3300
O'Sullivan, S. P., Lenc, E., Anderson, C. S., Gaensler, B. M., & Murphy, T. 2018, MNRAS, 475, 4263
Ozawa, T., Nakanishi, H., Akahori, T., et al. 2015, PASJ, 67, 110
Pearce, C. J. J., van Weeren, R. J., Andrade-Santos, F., et al. 2017, ApJ, 845, 81
Pearson, K. 1895, RSPS, 58, 240
Pizzo, R. F., de Bruyn, A. G., Bernardi, G., & Brentjens, M. A. 2011, A&A, 525, A104
Porter, D. H., Jones, T. W., & Ryu, D. 2015, ApJ, 810, 93
Robitaille, T., & Bressert, E. 2012, APLpy: Astronomical Plotting Library in Python, Astrophysics Source Code Library, ascl:1208.017
Roh, S., Ryu, D., Kang, H., Ha, S., & Jang, H. 2019, ApJ, 883, 138
Rybicki, G. B., & Lightman, A. P. 1986, Radiative Processes in Astrophysics (Weinheim: Wiley-VCH)
Ryu, D., Kang, H., Cho, J., & Das, S. 2008, Sci, 320, 909
Sokoloff, D. D., Bykov, A. A., Shukurov, A., et al. 1998, MNRAS, 299, 189
Stroe, A., Shimwell, T., Rumsey, C., et al. 2016, MNRAS, 455, 2402
Stuardi, C., Bonafede, A., Wittor, D., et al. 2019, MNRAS, 489, 3905
Tribble, P. C. 1991, MNRAS, 250, 726
van Weeren, R. J., Brüggen, M., Röttgering, H. J. A., & Hoeft, M. 2011, MNRAS, 418, 230
van Weeren, R. J., de Gasperin, F., Akamatsu, H., et al. 2019, SSRv, 215, 16
van Weeren, R. J., Röttgering, H. J. A., Brüggen, M., & Hoeft, M. 2010, Sci, 330, 347
van Weeren, R. J., Röttgering, H. J. A., Intema, H. T., et al. 2012, A&A, 546, A124
Vazza, F., Brunetti, G., Brüggen, M., & Bonafede, A. 2018, MNRAS, 474, 1672
Wittor, D., Hoeft, M., Vazza, F., Brüggen, M., & Domínguez-Fernández, P. 2019, MNRAS, 490, 3987